

Comparisons and Predictions for Collisions of deformed ^{238}U nuclei at $\sqrt{s_{NN}} = 193\text{ GeV}$

Nicolas Miro Fortier,^{1,*} Sangyong Jeon,^{1,†} and Charles Gale^{1,‡}

¹*Department of Physics, McGill University, 3600 University Street, Montreal, QC, H3A 2T8, Canada*

(Dated: June 17, 2024)

We present comparisons to experimental data along with predictions of observables for U+U and Au+Au collisions at 193 and 200 GeV respectively, using a multistage theoretical and computational framework consisting of boost-invariant IP-Glasma initial state, MUSIC hydrodynamics, and a hadronic transport cascade generated by iS3D & SMASH. Two different Woods-Saxon parametrizations were used for both systems [1, 2], allowing for comparisons within our model. Our results show great agreement with existing anisotropic flow measurements from RHIC [3, 4]. We provide predictions for differential flow observables as well as multiparticle correlations and transverse-momentum-flow correlations. When possible, we compare our predictions to results from Au+Au collisions at 200 GeV to properly outline the effects of deformation in the initial state on final state observables.

I. INTRODUCTION

Heavy-ion collisions at the Relativistic Heavy Ion Collider (RHIC) and the Large Hadron Collider (LHC) have provided remarkable insights into the fundamental properties of matter under extreme conditions [5]. One of the most intriguing phenomena observed in these collisions is the creation of quark gluon plasma (QGP), a state of matter characterized by the deconfinement of quarks and gluons [6]. The QGP, produced in the aftermath of collisions, exhibits collective behaviour reminiscent of a nearly perfect fluid. This remarkable hydrodynamic behaviour allows for the conversion of initial state anisotropies into final state observables, providing a unique window into not only the dynamics of the QGP, but also nuclear structure and its limits.

In studies involving spherically symmetric nuclei, researchers have extensively investigated the effects of specific subsets of initial state anisotropies resulting from nuclear geometry fluctuations. However, a significant gap remains in our understanding of the impact of initial state anisotropies originating from deformed nuclei, such as ^{238}U . These deformed nuclei introduce a wider range of anisotropies, presenting an opportunity to explore unique combinations of fluctuations and test certain phenomenological hypotheses within the QGP [7].

Notably, our study predicts that central collisions involving prolate-shaped nuclei (such as ^{238}U) should lead to a negative correlation between v_2 and p_T . In contrast, this correlation is observed to be positive at all centralities in collisions of spherical nuclei [8, 9]. Indeed, the prolate geometry of ^{238}U causes higher eccentricity (ε_2) events to generate lower $\langle p_T \rangle$ and vice-versa, inducing an anti-correlation of the two observables. These collisions also generate higher energy densities in ultra-central configurations compared to spherical nuclei. This extra energy density is expected to have observable effects on

various crucial observables, including elliptic flow and jet quenching [10], which serve as key probes to characterize the properties of the QGP, as well as collective properties and momentum correlations [11–13].

While considerable efforts have been made in studying heavy-ion collisions involving spherical nuclei [14–17], experimental data for collisions involving deformed nuclei (such as ^{238}U) remains limited. Furthermore, new studies have found that nuclei which had historically been modeled spherically (such as ^{197}Au) may actually be deformed [2, 11]. Therefore, not only do collisions of deformed nuclei present an exciting opportunity for testing our understanding of QGP dynamics, but ‘deformity’ may be more common than we believed in the nuclear world. To test these hypotheses, it is crucial to develop a comprehensive framework that can incorporate all types of fluctuations at all stages.

In this study, we employ an up-to-date, comprehensive and well-motivated theoretical framework to both compare to available data from STAR [3] and extract predictions for a wide range of observables in U+U and Au+Au collisions at $\sqrt{s_{NN}} = 193\text{ GeV}$ & 200 GeV respectively. Both collision systems will be studied using two distinct Woods-Saxon parametrizations each. Simulations begin with the IP-Glasma model, which is based on the Colour Glass Condensate (CGC) framework [18, 19] and provides realistic event-by-event colour fluctuations as well as pre-equilibrium flow. IP-Glasma has been successful at reproducing key observables across both the energy and collision system spectra [20–26]. MUSIC, a relativistic viscous hydrodynamic simulation which incorporates bulk and shear viscosities [27, 28], then takes over the evolution of the system. Once the density and temperatures of the QGP drop sufficiently, the system is ‘frozen-out’, meaning that fluid cells which were previously governed by hydrodynamics are converted into hadrons before being propagated. This final stage of the simulations is taken up by iS3D [29] & SMASH [30], two models which combine to generate hadronic cascades. The inner workings of the various phases of our simulations will be discussed in detail in section II.

This paper follows the following structure: section II

* nicolas.fortier@mail.mcgill.ca

† sangyong.jeon@mcgill.ca

‡ charles.gale@mcgill.ca

examines the different stages of our physical model in varying detail, ranging from an in-depth discussion of IP-Glasma in subsection II A to a more cursory look at hadronic transport model SMASH II C. Section III details the different studied observables and their working definitions, as well as theoretical expectations for their sensitivity to the initial state when possible. These include centrality selection (III A), flow analysis methods (III C 1) and transverse-momentum-flow correlations (III C 3). We then show our model's comparative and predictive capabilities and results in section IV. The paper will end with a summary and conclusion, presented in section V.

II. THEORETICAL MODEL

A. IP-Glasma

Historically, the first hydrodynamic models of heavy-ion collisions were developed with an emphasis on the fluid dynamics of QGP [31–42]. The initial states used by these first models were mainly geometric in nature [43]. Once the relevance and success of early heavy-ion collision simulations were established, the need for a more physically accurate and detailed initial state model became apparent. IP-Glasma, a QCD- and saturation-based model, was first introduced in 2012 [44] and quickly became the standard in the field. It is based on the Colour Glass Condensate (CGC) effective field theory [45–47] and classical gluon production [48–52].

To model heavy-ion collisions, one must first generate the nuclei. In this study, we use the deformed Woods-Saxon distribution, given by

$$\rho(r, \theta) = \frac{\rho_0}{1 + \exp\left(\frac{r - R(\theta, \phi)}{a}\right)} \quad (1)$$

$$R(\theta, \phi) = R_0 \left(1 + \sum_{l=2}^{l_{max}} \sum_{m=-l}^l \beta_l^m Y_l^m(\theta, \phi) \right) \quad (2)$$

to generate nucleon configurations. Here, ρ_0 denotes the nuclear density (which is calculated such that the Woods-Saxon distribution integrates to 1), R_0 is the unmodified nuclear radius and a is the nuclear skin depth. Real parameters β_l^m multiply the spherical harmonic functions $Y_l^m(\theta, \phi)$ and generate deformation about the x and y axes. The parameters used in this study of ^{238}U and ^{197}Au are presented in Tab. I. We see that all deformed parametrizations include quadrupole ($l = 2$) and hexadecapole ($l = 4$) moments, while others associated with triaxiality γ are only included for the Deformed ^{197}Au parametrization, as no evidence currently suggests that such parameters are relevant for ^{238}U . A comparison between an undeformed and a deformed nucleus using the parameters used in this study is presented in Fig. 1.

The Woods-Saxon distribution is a simplistic yet effective model for sampling nucleon positions, as evidenced

TABLE I. Deformed Woods-Saxon parameters used for sampling nuclei according to Eq. 2, taken from [1] (Prev ^{238}U and Spherical Au) and [2] (New ^{238}U and Deformed Au).

	New ^{238}U	Prev ^{238}U	Spher ^{197}Au	Def ^{197}Au
R_0 (fm)	7.068	6.874	6.37	6.62
a (fm)	0.538	0.556	0.535	0.519
β_2^0	0.247	0.2802	0	0.098
β_2^2	0	0	0	0.076
β_4^0	0.081	-0.0035	0	-0.025
β_4^2	0	0	0	-0.018
β_4^4	0	0	0	-0.018

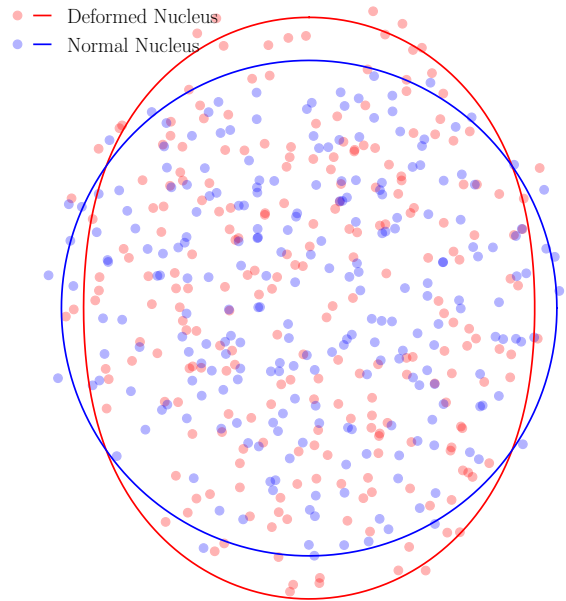


FIG. 1. Comparing a regular and deformed Woods-Saxon distribution with same base radius R_0 and skin depth a (set to that of Prev ^{238}U in Tab. I). The deformed distribution generates an oblong (or pill-shaped) profile. The rotational symmetry axis is the long vertical axis.

by its widespread use in the field. However, as with any simple model, one must understand its limitations. The β_l^m deformation parameters are model-dependent, in so far as their extraction must figure in the Woods-Saxon distribution. Also, the distribution itself does not account for important nucleon-nucleon correlations, which more recent studies have shown to have sizable effects in generating physically accurate nuclei configurations [53, 54]. Therefore, it should be understood that all of the results presented in this paper carry an inherent systematic uncertainty.

Following nucleon sampling, the impact parameter for the event is sampled from

$$P(b)db = \frac{2b}{b_{\max}^2 - b_{\min}^2} db \quad (3)$$

where $b_{\max} = 8 \text{ fm}$ and $b_{\min} = 0 \text{ fm}$. The boundaries were fixed with the goal of rejecting as few events as possible due to their peripherality since deformation effects are only tangible in central collisions of deformed nuclei. The nuclei configurations are then shifted symmetrically by $b/2$ in the x -direction. The spatial distribution of nucleons is then projected into the transverse plane.

At this point, IP-SAT [55], the impact parameter dependent dipole saturation model, takes over. Its contribution will be in providing the saturation scale Q_s at all points in the transverse plane, which then allows us to sample colour charges and initialize the system's colour gauge fields. To do so, IP-SAT first models the nuclear thickness function as

$$T(\mathbf{x}) = \frac{e^{-\mathbf{x}^2/2B_G}}{2\pi B_G} \quad (4)$$

$$T_A(\mathbf{x}) = \sum_{i=1}^A T(\mathbf{x} - \mathbf{x}_i) \quad (5)$$

where A represents the current nucleus' number of nucleons and $B_G = 4.0 \text{ GeV}^{-2}$ is extracted from a fit to DIS data [56]. With the thickness function for each nucleus in hand, we solve

$$\frac{2\pi^2}{N_c} T_{A,B}(\mathbf{x}) r_s^2 x g(x, \mu^2(r_s^2)) \alpha_s(\mu^2(r_s^2)) = 1 \quad (6)$$

for $Q_s^2 = 2/r_s^2$, where $N_c = 3$ is the number of colours permitted and $T_{A,B}(\mathbf{x})$ is the thickness function described in Eq.(5) for the projectile (A) and target (B) nuclei. $xg(x, \mu^2)$, the density of gluons at a given scale μ and momentum fraction x , is initialized as

$$xg(x, \mu_0^2) = A_g x^{\lambda_g} (1-x)^{5.6} \quad (7)$$

with $A_g = 2.308$, $\lambda_g = 0.058$ and $\mu_0^2 = 1.51 \text{ GeV}^2$. Eq.(7) is then evolved to all other values of μ^2 using the leading-order DGLAP equation [57–59]. The scale μ itself is related to the saturation dipole size (and scale) by

$$\mu^2 = \frac{4}{r_s^2} + \mu_0^2 = 2Q_s^2 + \mu_0^2 \quad (8)$$

which sets the scale in the leading-order QCD running coupling constant given by

$$\alpha_s(\mu^2) = \frac{12\pi}{(33 - 2N_f) \ln\left(\frac{\mu^2}{\Lambda_{QCD}^2}\right)}. \quad (9)$$

where N_f is the number of quark flavours, set to 4 in our simulation. Eq.(6) is itself extracted from the Glauber-Mueller dipole cross-section [60]. Solving for Q_s must be done iteratively given the intricate interdependence of the various functions (xg , α_s) and variables (x , r_s , μ , Q_s).

Once Q_s^2 is determined, the colour charge distribution for the projectile nucleus, for instance, can be sampled from the following colour correlator

$$\langle \rho_A^a(\mathbf{x}) \rho_A^b(\mathbf{y}) \rangle = g^2 \mu_A^2(\mathbf{x}, \mathbf{x}) \delta^{ab} \delta^2(\mathbf{x} - \mathbf{y}), \quad (10)$$

where x is the momentum fraction currently considered and $Cg^2\mu_A = Q_s^4$ ¹. We are therefore sampling from a Gaussian of width proportional to the saturation scale. The proportionality constant C is determined phenomenologically and was set to 0.505 in this study.

This sampled colour charge distribution is of great importance, as it acts as a source for the small- x gluon fields which comprise the CGC. The CGC action,

$$S_{CGC} = \int d^4x \left(-\frac{1}{4} F_{\mu\nu}^a F_a^{\mu\nu} + J^{\mu a} A_\mu^a \right) \quad (11)$$

contains a current term $J^{\mu a}$ which sources the colour gauge fields A_μ^a . The convention for the covariant derivative and, therefore, the field strength tensor used throughout this paper is

$$D_\mu = \partial_\mu + ig A_\mu$$

$$F_{\mu\nu} = \partial_\mu A_\nu - \partial_\nu A_\mu + ig [A_\mu, A_\nu].$$

The corresponding Classical Yang-Mills (CYM) equation is

$$[D_\mu, F^{\mu\nu}] = J^\nu \quad (12)$$

where

$$J^\nu = \rho_A(\mathbf{x}) \delta^{\nu+} \delta(x^-) \quad (13)$$

Here, the two δ -functions indicate a right-moving source on the light cone. Note the move to light-cone coordinates $x^\pm = (t \pm z)/\sqrt{2}$, meaning that our sources (large- x partons) are travelling at the speed of light. In the pre-collision phase, the CYM equations in the $A_- = 0$ gauge are

$$\nabla_\perp^2 A_+^a = -\rho^a \quad (14)$$

which are Poisson equations for each colour index. The more physical light-cone gauge gluon fields can be obtained by a gauge transformation

$$A_\mu^A = V^A A_\mu V^{A\dagger} - \frac{i}{g} V^A \partial_\mu V^{A\dagger} \quad (15)$$

where

$$V(x^-, \mathbf{x}) = \mathcal{P} \exp \left(-ig \int_{-\infty}^{x^-} dy^- A_-(y^-, \mathbf{x}) \right) \quad (16)$$

In this 2D setting, only the transverse components A_x^A and A_y^A are non-zero.

¹ It is important to note here that $\mu_A \neq \mu$. μ is the intrinsic energy scale at hand, while μ_A is the scale of colour charge fluctuations, which is related to the saturation scale.

Once the pre-collision colour gauge fields have been determined, the collision takes place; both fields are combined such that the forward light cone has the following initial fields

$$A_i = A_i^A + A_i^B \quad (17)$$

$$E^\eta = ig [A_i^A, A_i^B], \quad (18)$$

where $i = x, y$. The dynamics inside the forward light cone are best described using $\tau - \eta$ coordinates, which we will use in the rest of this work. To obtain the other components of the chromo-electric field E^i , we must solve the covariant form of Gauss' law,

$$[D_i, E^i] + [D_\eta, E^\eta] = 0. \quad (19)$$

Since derivatives in η vanish in our boost-invariant implementation, we are left with $[D_i, E^i] = 0$, which has trivial solution $E^i = 0$: the initial transverse chromo-electric fields are therefore set to 0 [61, 62].

Once the initial post-collision fields are settled, we evolve the whole system using the sourceless CYM equations,

$$[D_\mu, F^{\mu\nu}] = 0 \quad (20)$$

until $\tau_{\text{hyd}} = 0.52 \text{ fm}$. At that time, the CYM stress-energy tensor, given by

$$T^{\mu\nu} = \text{Tr} \left(-g^{\mu\gamma} g^{\nu\alpha} g^{\beta\delta} F_{\gamma\beta} F_{\alpha\delta} + \frac{1}{4} g^{\mu\nu} g^{\gamma\beta} g^{\alpha\delta} F_{\gamma\alpha} F_{\beta\delta} \right) \quad (21)$$

is constructed. It is symmetric and gauge invariant, and is the bridge that connects the pre-equilibrium dynamics of the glasma to the relativistic hydrodynamics of the QGP. We refer to [63] for an in-depth discussion about the properties and development of the tensor. To find the energy density ε and flow velocity u^μ , we diagonalize $T^{\mu\nu}$ and preserve the timelike eigenvalue. The flow velocity is normalized to $u_\mu u^\mu = 1$ throughout.

The shear-stress tensor $\pi^{\mu\nu}$, which is needed to initialize viscous hydrodynamics, is given by

$$\pi^{\mu\nu} = T_{\text{IPG}}^{\mu\nu} - T_{\text{ideal}}^{\mu\nu} \quad (22)$$

$$T_{\text{ideal}}^{\mu\nu} = (\varepsilon + P)u^\mu u^\nu - P g^{\mu\nu} \quad (23)$$

In IP-Glasma, the pressure P is given by $\varepsilon/3$ due to the conformality of the classical gluon system. The conformal nature of the pre-equilibrium phase, originating from the pure gluon and classical features of the CGC, also justifies the absence of a bulk pressure Π at this stage. On the hydro side, the pressure is dictated by the EoS at use, which in this study is HotQCD [64]. An issue arises when one realises that $P_{\text{IPG}} = \varepsilon/3$ and $P_{\text{EoS}}(\varepsilon)$ may not match, leading to a discontinuity in our transition to hydrodynamics. This issue is handled by initializing the QGP with a bulk pressure Π , which, at this point, is required and given by the difference between the IPG and EoS pressures, i.e.

$$\Pi = P_{\text{IPG}}(\varepsilon) - P_{\text{EoS}}(\varepsilon) = \frac{\varepsilon}{3} - P_{\text{EoS}}(\varepsilon) \quad (24)$$

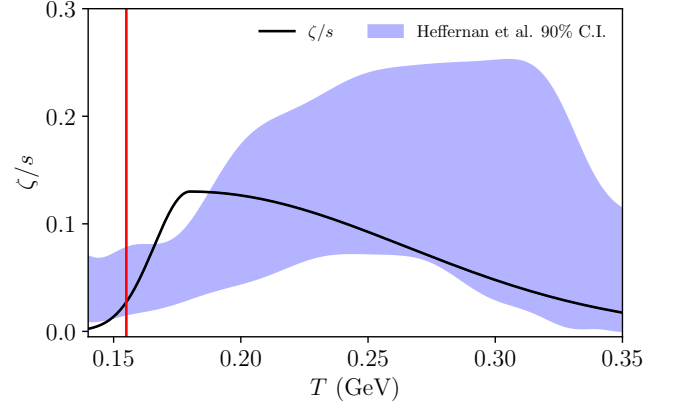


FIG. 2. Bulk viscosity to entropy density ratio ζ/s as a function of temperature. The red vertical line shows the freeze-out temperature ($T_{sw} = 155 \text{ MeV}$) below which iS3D & SMASH, our hadronic transport models, take over.

We therefore fully conserve energy and momentum in our transition to hydrodynamics, which allows for proper tracking and accounting of quantities such as $dE/d\eta$ from the initial state into the hydrodynamics phase.

B. MUSIC

While the CGC is an effective *field* theory, hydrodynamics is a long-wavelength effective theory [65, 66]. Both, however, have the same objective: to describe reality as efficiently and accurately as possible, while providing pragmatic theories which allow for the extraction of usable results. In the hydrodynamics phase, the evolution shifts from more fundamental degrees of freedom such as the gluon fields to coarse-grained thermodynamic ensemble averages, such as pressures and temperatures.

MUSIC [27, 67] is the numerical implementation of the following theoretical concepts. Formally, it is a second-order relativistic viscous hydrodynamics simulation. The fundamental quantity being evolved in hydrodynamics is the energy-momentum tensor

$$T_{\text{Hydro}}^{\mu\nu} = T_{\text{ideal}}^{\mu\nu} + \Pi(u^\mu u^\nu - g^{\mu\nu}) + \pi^{\mu\nu} \quad (25)$$

In second order viscous hydrodynamics, the conservation laws

$$\partial_\mu T_{\text{Hydro}}^{\mu\nu} = 0 \quad (26)$$

are supplemented by equations of motion for the viscous tensor $\pi^{\mu\nu}$ and the bulk pressure Π

$$\dot{\Pi} = \frac{1}{\tau_\Pi} (-\Pi - \zeta\Theta - \delta_{\Pi\P}\Pi\Theta) \quad (27)$$

$$\dot{\pi}^{\langle\mu\nu\rangle} = \frac{1}{\tau_\pi} (-\pi^{\mu\nu} + 2\eta\sigma^{\mu\nu} - \delta_{\pi\pi}\pi^{\mu\nu}\Theta) \quad (28)$$

Here, $\Theta = \partial_\mu u^\mu$ is the scalar expansion rate and $\sigma^{\mu\nu} = \nabla^{\langle\mu} u^{\nu\rangle}$ is the velocity shear tensor. The overdot represents the co-moving frame time derivative $u^\mu \partial_\mu$ and the angular bracket around the indices indicate the transverse, symmetric and traceless part of the tensor. The coefficients $\delta_{\Pi\Pi}/\tau_\Pi$ and $\delta_{\pi\pi}/\tau_\pi$ are derived using the 14-moment approximation, whose values are 2/3 and 4/3 respectively, according to [68]. The bulk viscosity ζ and the shear viscosity η have the following form

$$\frac{\zeta}{s}(T) = N \exp\left(-\frac{(T - T_p)^2}{B_{(L,G)}^2}\right) \quad (29)$$

$$\frac{\eta}{s} = 0.136 \quad (30)$$

where s is the entropy density and the energy unit is GeV. In this study, following the Bayesian analysis performed in [23], we have opted to use a constant shear viscosity η/s and a temperature-dependent bulk viscosity ζ/s . Eq.(29) shows the functional form of ζ/s , where $N = 0.13$ and $T_p = 0.18$ GeV. The width $B_{(L,G)}$ depends on whether the temperature of the QGP is smaller or larger than the bulk peak temperature T_p : if $T < T_p$, we have $B_L = 0.02$ GeV, while $B_G = 0.12$ GeV is used for $T > T_p$. The form of the bulk is therefore that of an asymmetrical gaussian distribution, with features specifically chosen to avoid large bulk viscous corrections at freeze-out, as described in [22]. Fig. 2 shows Eq. (29) compared to the posterior 90% confidence interval inferred in the above-mentioned Bayesian analysis [23]. Our curve falls within the interval for most of the relevant temperature range. While its peak does fall outside of the confidence interval, our parametrization remains fully consistent with the findings of the analysis. In Bayesian analysis, a 90% confidence interval provides a general region of space where a certain parameter should lie, while still allowing some part of the parameter curve to lie outside of it. Given that the beam energies considered in this work are much smaller than those considered in [23], our results are more sensitive to low-temperature bulk features. The bulk viscosity we have used reflects this sensitivity, while preserving consistency with the Bayesian analysis in [23]. With time, the QGP grows in volume while its temperature drops. At a certain temperature, the QGP will ‘hadronize’, i.e. turn into hadrons. The exact value of this temperature is not sharply defined [69–71]. In this study, the switching temperature is set to $T_{\text{sw}} = 155$ MeV. Once a specific fluid cell cools down to temperature T_{sw} , its spatiotemporal state is saved. Once every fluid cell has reached T_{sw} , all of the 4-dimensional states are combined to generate a constant-temperature hyper-surface, which terminates the hydrodynamic stage of the simulation.

C. iS3D & SMASH

The freeze-out hyper-surface generated by MUSIC is fed into iS3D [29], a particlization code which implements

Cooper-Frye sampling [72], i.e.

$$E \frac{dN_i}{d^3p} = \frac{d_i}{(2\pi)^3} \int_\Sigma f_i(x, p) p_\mu d\sigma^\mu(x) \quad (31)$$

where Σ is an isothermal hyper-surface and $\sigma^\mu(x)$ is its normal vector, $E \frac{dN_i}{d^3p}$ is the momentum spectrum of particle species i , $f_i(x, p)$ is its phase-space distribution and d_i is the degeneracy factor. To ensure a smooth transition between hydrodynamics and particlization, the energy-momentum tensor $T^{\mu\nu}$ must be reproduced everywhere on the hyper-surface. Therefore,

$$T_{\text{kin}}^{\mu\nu} = \sum_i d_i \int \frac{d^3p}{(2\pi)^3} E p^\mu p^\nu (f_{\text{eq},i}(x, p) + \delta f_i(x, p)) \quad (32)$$

where $f_i(x, p)$ has been decomposed into an equilibrium distribution (which follows either Bose-Einstein or Fermi-Dirac statistics depending on the species i) and an out-of-equilibrium correction δf_i . This correction is necessary to account for the viscous nature of our hydrodynamic evolution. Indeed, these lead to a medium which is out-of-equilibrium at the time of sampling which in turn produces slight deviations from the equilibrium distributions $f_{\text{eq},i}$. To match the nature of our shear stress $\pi^{\mu\nu}$ and bulk viscous pressure Π , we use the 14-moment δf_i corrections. It is an expansion of δf_i which is truncated at terms of first- and second-order in momentum (p^μ and $p^\mu p^\nu$) [73–75].

An important concept, which will be revisited in more detail in subsection III B, is the fact that the freeze-out hyper-surface from a single hydrodynamic event is oversampled hundreds of times [22–24]. Indeed, because the hyper-surface stems from a hydrodynamic treatment of the QGP, which itself is an ensemble average, the sampling of particles will converge to the hydrodynamic value of all observables (multiplicity, momenta, flow) only once a sufficient number of samplings are done. Therefore, a single IP-Glasma and MUSIC event, comprised of a unique collision, impact parameter and nuclei configuration, can generate hundreds of iS3D events, each consisting of its own particle list containing specific species and momenta. In this work, we test two different ways of treating these oversampled events. The oversampled events from a single hydrodynamic event can be averaged over and treated as a single event, relating it to its initial and hydrodynamic stages uniquely. Alternatively, each oversampled event can be regarded as a distinct event fitting the general prescription provided by the ensemble average hyper-surface. Choosing one method over the other has tangible effects on computed observables, as will be evidenced in our results.

Once the hadrons are sampled, they are evolved kinetically using SMASH [30], a hadronic cascade code. It implements inter-particle interactions and scatterings, as well as resonance and decays via coupled Boltzmann equations of most of the known hadrons. We used SMASH Version 1.8 in this work.

III. METHODS AND OBSERVABLES

A. Centrality

Proper centrality selection is key to ensuring that the theoretical and computational models of HICs are comparable to available experimental data. In this study, matching multiplicities across centrality classes served as the sole calibration of our model: the proportionality constant $C = 0.505$, described in section II A, was calibrated to reproduce U+U multiplicity distributions at 193 GeV following the approach advocated in [24] and described below. This is the only calibration we made. All observables extracted thereafter used this calibrated value.

When all events have gone through all stages of our framework, they are sorted by charged particle multiplicity $dN_{\text{ch}}/d\eta$, then separated into a sufficiently many number of bins, all of which contain the same number of events. The C parameter is calibrated such that the average multiplicity of the most central bin matches that of experiment. Two experimental centrality bins and their respective multiplicities are then selected. These are the most central and the most peripheral centrality we would like to analyze (in this study, 0 – 1% and 27 – 28% respectively). The experimental multiplicity ratios of these two bins is then computed. The same is done with the first and last bins from the simulations. While the ratio of the average multiplicities of our two selected bins exceeds that of the corresponding experimental ratio, we drop the lowest-multiplicity event from our consideration, recalculate the ratio, and keep repeating this until the desired ratio is achieved, allowing us to reject a negligible number of events compared to what would have to be rejected in a fully minimally-biased study. The calibration and peripheral event dropping steps are sufficient to ensure that we reproduce available charged hadron multiplicity curves (see Fig. 3 below), which then allows for a thorough comparison to all available observables.

Another important aspect of this study was the faithful emulation of Zero-Degree Calorimeter (ZDC) binning to compare to data from STAR [3]. The ZDC is a calorimeter that resides at 0° from the beam direction. It aims to measure neutrons which were a part of the colliding nuclei, but did not participate in the collision. Their lack of electric charge means that once they are free from the confines of their nucleus, the collider’s electromagnetic fields do not affect them, leading them to follow straight paths directly into the calorimeters.

Experimentalists assess the centrality of a collision by counting the number of detected neutrons: the more neutrons were found, the higher the chance that the collision was peripheral. To emulate ZDCs within our framework, we calculate the total number of participating nucleons from a given collision event and subtract it from the total number of nucleons available to give us the number

of spectator nucleons S , i.e.

$$S = 2A - N_{\text{Participants}} \quad (33)$$

where $A = 238$ for a U+U collision. To obtain the number of neutrons out of the total number of spectator nucleons, we sample a binomial distribution

$$P(N) = \binom{S}{N} \left(1 - \frac{Z}{A}\right)^N \left(\frac{Z}{A}\right)^{S-N} \quad (34)$$

where Z is the atomic number (92 for U) and we aim to sample N , the number of neutrons, as done in [76]. We average 20 samplings of this distribution per event to reduce variability, giving us the number of spectator neutrons for each event. This method does overlook some points, such as the fact that atomic nuclei have neutron skins (an outer shell where only neutrons are found) [77, 78] which lead to higher probabilities of having spectator neutrons than protons which aren’t encapsulated within our simple binomial distribution. These considerations, however, were outside of the scope of this study.

B. Averaging

In section II C, we briefly discussed the concept of oversampling the hydrodynamical hyper-surface. Given the ensemble average definition of this hyper-surface, sampling it multiple times is an important part of ensuring that the final state observables associated with an event converge to their hydrodynamic values. Previously [22–24], this oversampling procedure (which, in this work, we will call ‘oversampled average’) is followed by an averaging of the oversampled events to create a single set of observables related to a single hyper-surface. By design, this method smoothes out fluctuations and accentuates the features associated with a given hyper-surface. If, however, each oversampled event is regarded as an independent event and averaging is only performed in a given centrality class, the effects of short-range fluctuations and correlations will remain (we will call this method ‘SMASH sub-event averaging’). However, events that came from the same hyper-surface event may not be fully independent. Not all observables are sensitive to these differing averaging methods. But, as will become evident in our results section, many observables studied in this work *are* sensitive to the averaging method.

An ideal simulation of one experimental event would be the chain of one IP-Glasma, one hydro, and one SMASH event. This, however, requires many orders of magnitude more computing resources than are currently available. As such, it is important to analyze which observables are sensitive and for what reasons, as we have done in this study. For this purpose, we also compare the above two averaging methods to the ‘mixed events’ in Section IV, where we group all oversampled events from a given centrality class, mix all of their particles and create new ‘mixed’ events. Only un-correlated fluctuations should survive in these mixed events.

C. Defining Selected Observables

The following parts will briefly introduce and define a selection of the observables which will figure in our results in section IV.

1. Flow analysis

The n -th anisotropic flow coefficient v_n is by now generally accepted as one of the primary evidence of QGP undergoing fluid-like behaviour in relativistic heavy-ion collisions. In this study, we will be interested in the 2- and 4-particle cumulants of various components of the flow harmonics. To start, we define the flow vector Q_n for each event [79],

$$Q_n = \sum_{j=1}^{N_{\text{ch}}} e^{in\phi_j} \quad (35)$$

where N_{ch} is the event's multiplicity, j runs over all of the particles of the event with transverse momentum restricted to $0.2 \text{ GeV} < p_T < 2.0 \text{ GeV}$ to conform with the STAR acceptance window, and ϕ_j is the azimuthal angle of the j^{th} particle. Then, the 2nd order azimuthal correlation is given by

$$\langle 2 \rangle = \frac{|Q_n|^2 - N_{\text{ch}}}{N_{\text{ch}}(N_{\text{ch}} - 1)} \quad (36)$$

while the 4th order azimuthal correlation is

$$\langle 4 \rangle = \frac{|Q_n|^4 + |Q_{2n}|^4 - 2 \text{Re}[Q_{2n} Q_n^* Q_n^*]}{N_{\text{ch}}(N_{\text{ch}} - 1)(N_{\text{ch}} - 2)(N_{\text{ch}} - 3)} - 2 \frac{2(N_{\text{ch}} - 2) \cdot |Q_n|^2 - N_{\text{ch}}(N_{\text{ch}} - 3)}{N_{\text{ch}}(N_{\text{ch}} - 1)(N_{\text{ch}} - 2)(N_{\text{ch}} - 3)}. \quad (37)$$

where Q_{2n} is to be understood as the flow vector associated with the $2n$ -th harmonic if we are calculating the 4th order azimuthal correlation of the n -th harmonic (i.e. if $n = 2$, then $Q_{2n} = Q_4$). We then take an average of these correlations over the entirety of events in their centrality class, which finally allows us to compute the 2- and 4-particle cumulants, i.e.

$$v_n\{2\} = \sqrt{\langle \langle 2 \rangle \rangle} \quad (38)$$

$$v_n\{4\} = \sqrt[4]{-\left(\langle \langle 4 \rangle \rangle - 2 \cdot \langle \langle 2 \rangle \rangle^2\right)} \quad (39)$$

where $\langle \langle \cdot \rangle \rangle$ denotes $\langle \cdot \rangle$ averaged over the given centrality.

Finally, the 2-particle scalar product p_T -differential flow is given by

$$v_n\{2\}(p_T) = \frac{\text{Re}(\langle Q_n^{\text{PI}}(p_T) \cdot (Q_n^{\text{ref}})^* \rangle)}{\langle N_{\text{ch}}^{\text{PI}}(p_T) N_{\text{ch}}^{\text{ref}} \rangle v_n^{\text{ref}}\{2\}} \quad (40)$$

where the superscript ‘PI’ denotes the particle species of interest, while the superscript ‘ref’ denotes the reference

flow vector. To avoid self-correlations being represented in this observable, Q_n^{PI} is taken from the $|\eta| < 0.5$ rapidity window, while the reference flow vector is taken from $0.5 < \eta < 2$.

For a more thorough treatment and discussion of these quantities, along with their respective errors, see [80].

2. Multi-particle Transverse Momentum Correlators

We will be presenting results for 2- and 3-particle p_T correlations, which are sometimes referred to as ‘variance’ and ‘skewness’ respectively, the difference being that the correlators do not consider self-correlations. The event-averaged 2-particle transverse momentum correlator is defined as

$$\langle \delta p \delta p \rangle = \left\langle \frac{\sum_{i \neq j} (p_i - \langle p_T \rangle)(p_j - \langle p_T \rangle)}{N_{\text{ch}}(N_{\text{ch}} - 1)} \right\rangle \quad (41)$$

where the sum is over particles in a given event, the averaging is over the given centrality class and $\langle p_T \rangle$ denotes the average transverse momentum in the centrality class being analyzed. The 3-particle version is

$$\langle \delta p \delta p \delta p \rangle = \left\langle \frac{\sum_{i \neq j \neq k} (p_i - \langle p_T \rangle)(p_j - \langle p_T \rangle)(p_k - \langle p_T \rangle)}{N_{\text{ch}}(N_{\text{ch}} - 1)(N_{\text{ch}} - 2)} \right\rangle \quad (42)$$

where $\langle p_T \rangle$ denotes the average transverse momentum over the centrality class being analyzed. Implementing these formulae numerically as they are presented would be unwise, as they would run at least in $O(N_{\text{events}} \cdot N_{\text{ch}}^2)$ and $O(N_{\text{events}} \cdot N_{\text{ch}}^3)$ respectively. To avoid such computationally taxing and redundant computations, we have implemented a modified version of a framework presented by Giacalone et al. [81]. We start by defining P_n , the modified moments of the p_T distributions,

$$P_n = \sum_i^{N_{\text{ch}}} (p_i - \langle p_T \rangle)^n \quad (43)$$

where p_i is the transverse momentum of the i^{th} particle in the given event. Then one can easily show

$$\sum_{i \neq j} (p_i - \langle p_T \rangle)(p_j - \langle p_T \rangle) = (P_1)^2 - P_2 \quad (44)$$

$$\sum_{i \neq j \neq k} (p_i - \langle p_T \rangle)(p_j - \langle p_T \rangle)(p_k - \langle p_T \rangle) = (P_1)^3 - 3P_2P_1 + 2P_3 \quad (45)$$

allowing for the following redefinitions of the 2- and 3-particle transverse momentum correlators

$$\langle \delta p \delta p \rangle = \left\langle \frac{(P_1)^2 - P_2}{N_{\text{ch}}(N_{\text{ch}} - 1)} \right\rangle \quad (46)$$

$$\langle \delta p \delta p \delta p \rangle = \left\langle \frac{(P_1)^3 - 3P_2P_1 + 2P_3}{N_{\text{ch}}(N_{\text{ch}} - 1)(N_{\text{ch}} - 2)} \right\rangle \quad (47)$$

All of the modified moments are computable in linear time on an event-by-event basis, greatly reducing the computational stress required to extract such observables from large particle lists. Also, since both quantities have been reduced to a single term compared to the moments presented in [81], the calculation of their respective errors has been greatly simplified.

3. Transverse-momentum-flow correlations

The final selected observable integrates both the flow harmonics and the 2-particle transverse momentum correlator. It is a correlator between 2-particle flow harmonics and average transverse momentum which was developed in [82]. It is defined as

$$\rho(v_n\{2\}^2, \langle p_T \rangle) = \frac{\text{cov}(v_n\{2\}^2, \langle p_T \rangle)}{\sqrt{\text{var}(v_n^2) \cdot \langle \delta p \delta p \rangle}} \quad (48)$$

where

$$\text{cov}(v_n\{2\}^2, \langle p_T \rangle) = \left\langle \frac{|Q_n|^2 - N_{\text{ch}}}{N_{\text{ch}}(N_{\text{ch}} - 1)} \cdot \left(\frac{\sum_{i=1}^{N_{\text{ch}}} p_i}{N_{\text{ch}}} - \langle p_T \rangle \right) \right\rangle \quad (49)$$

and

$$\text{var}(v_n^2) = v_n\{2\}^4 - v_n\{4\}^4 \quad (50)$$

This correlator will be important in highlighting specific properties of central collisions of deformed nuclei. Indeed, it should show marked differences when compared to results from collisions of spherically symmetric nuclei.

IV. RESULTS AND DISCUSSION

Our results section will be divided into two subsections; the first contains comparisons of our model to existing data from two RHIC detectors (STAR and PHENIX) for U+U collisions at $\sqrt{s_{NN}} = 193$ GeV when available and Au+Au collisions at $\sqrt{s_{NN}} = 200$ GeV otherwise, while the second will focus on predictions of our model regarding multiparticle correlations and transverse-momentum-flow correlations in U+U collisions.

A. Descriptions of Existing Data

1. Charged Hadron Multiplicity

We begin by verifying that our model can reproduce charged hadron multiplicity at midrapidity. As mentioned in section III A, this observable serves as the sole calibration tool for the proportionality constant between the saturation scale Q_s and colour charge fluctuations

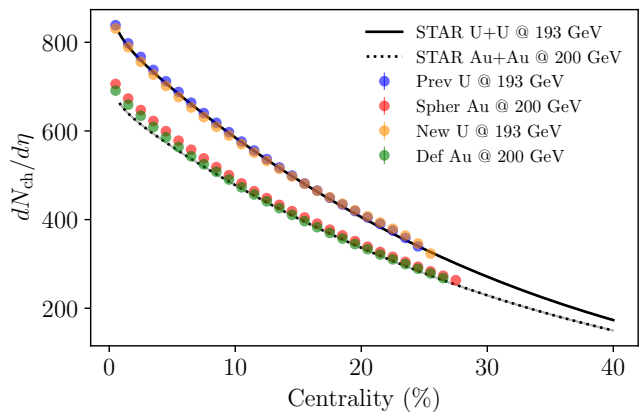


FIG. 3. Charged hadron multiplicities in $|\eta| < 0.5$ as a function of centrality in our model, compared to results for 193 GeV U+U and 200 GeV Au+Au collisions at STAR [3].

μ_A . The proportionality constant was calibrated using U+U experimental data and the Prev ^{238}U parametrization Tab. I.

In Fig. 3, we show the number of charged particles per unit pseudo-rapidity $dN_{\text{ch}}/d\eta$ from our model compared to data from STAR at 193 GeV (U+U) and 200 GeV (Au+Au). The experimental data stems from a parametrization undertaken in [3]. Our model's agreement with the U+U and Au+Au data is excellent throughout, with the Au data showing a slight overestimate of the multiplicity in central collisions. Comparing both systems' curves, we find that their features are similar beyond the fact that U collisions yield more hadrons, which is sensible given their larger nucleonic content (and, consequently, their larger total collision energy).

For the U parametrizations, the most peripheral point, at 25–26% centrality, dips slightly compared to the rest of our curve. This is due to our centrality selection procedure outlined in section III A. Indeed, our procedure is bound to allow for events which are ‘too’ peripheral to be found in our most peripheral bin, given that we reject events based on multiplicity (and, therefore, peripherality) until the multiplicity ratio matches that of the experiment. The Au parametrizations, on the other hand, do not feature this same dip, as the size of Au nuclei (spherical or deformed) is smaller than that of U nuclei. Therefore, given the impact parameter range used in this study ($0 \text{ fm} \leq b \leq 8 \text{ fm}$), our raw Au data actually extended beyond the 25% maximum centrality of our U calculation. We elected to apply our centrality selection procedure with a similar target range as our U data, as more peripheral data would not be of use in our analysis. This meant that our centrality selection cut a considerable amount of Au events off, but it also meant that it was more robust, as this centrality point's associated impact parameter interval was well-within our chosen impact parameter range. It is clear that, for both collision

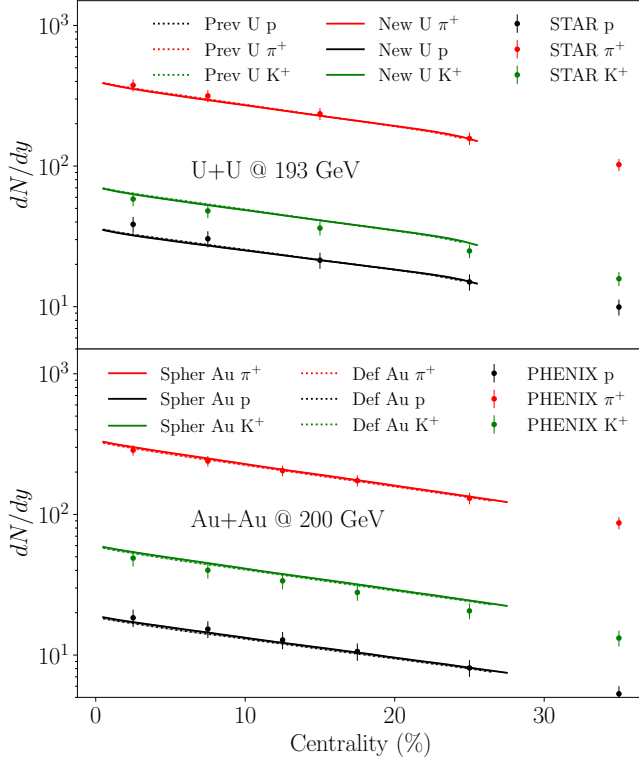


FIG. 4. Identified particle multiplicity in $|y| < 0.5$ as a function of centrality in our model. **(Top)** Two U configurations compared to results for 193 GeV U+U collisions at STAR [83]. **(Bottom)** Two Au configurations compared to results for 200 GeV Au+Au collisions at PHENIX [84].

systems, the choice of parametrization has little effect on multiplicity across the entire range, with the largest difference being in central (0 – 5% centrality) collisions of Au nuclei. This overestimate, both in scale and in position, is not surprising given that differences between parametrizations are exacerbated in central collisions and that our calibration was U-specific.

Our relatively narrow centrality window ($\sim 0 - 25\%$) is due to a conscious choice and focus: the differences between collisions of deformed nuclei and collisions of spherical nuclei are most prominent in central collisions. We sought to limit our scope to more central collisions to generate sufficient statistics in the region of interest without using computational resources to simulate more peripheral events where the differences are not particularly noticeable.

Fig. 4 shows identified particle yields as a function of centrality compared to data from STAR [83] and PHENIX [84]. All species considered, our calculation shows great agreement across the entire centrality window for all configurations and collision systems. To mirror experimental procedures used at STAR [83], the pion yields were corrected for feed-downs, while proton yields were not. When compared to PHENIX data [84], both proton and pion yields were corrected for feed-downs. It

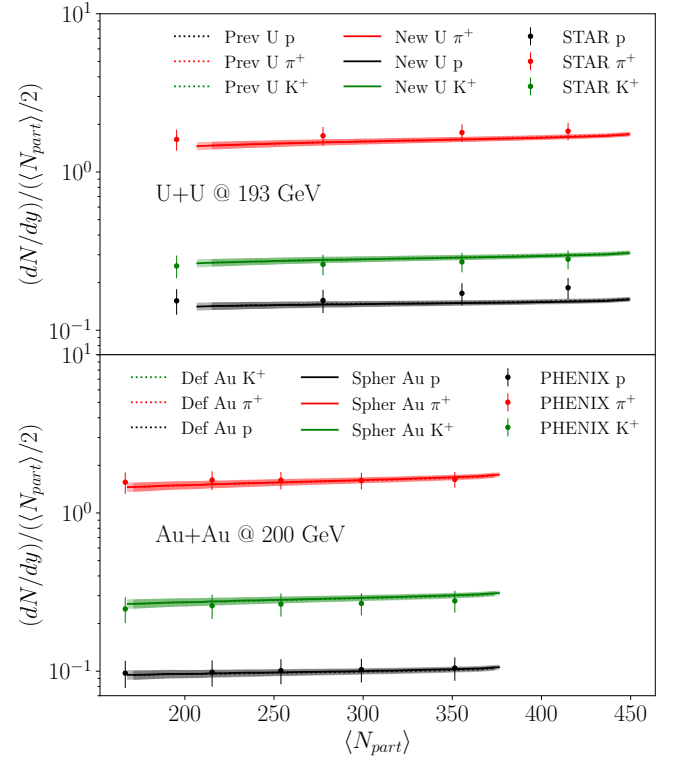


FIG. 5. Identified particle multiplicity in $|y| < 0.5$ scaled by average number of participant nucleon pairs in the centrality class $\langle N_{part} \rangle / 2$ as a function of $\langle N_{part} \rangle$ in our model. **(Top)** Two U configurations compared to results for 193 GeV U+U collisions at STAR [83]. **(Bottom)** Two Au configurations compared to results for 200 GeV Au+Au collisions at PHENIX [84].

is important to note here that our model does not include a baryon chemical potential. At this collision energy, μ_B is small but non-zero. Given that charged particle multiplicities were quasi-identical across different configurations, it is not surprising that identified particle yields behave similarly.

Fig. 5 shows identified particle yields scaled by the average number of participant nucleon pairs in a given centrality class $\langle N_{part} \rangle / 2$ as a function of the number of participants. This set of results is dependent on the results shown in Fig. 4, as the number of participant nucleons and centrality are highly correlated. However, this specific observable looks to identify where particle production comes from at a given centrality, and how it progresses across the spectrum. Because it increases with the average number of participant nucleons, we determine that particle production is guided by a combination of soft and hard processes that scale differently with N_{part} . Here again, both configurations for both collision systems give quasi-identical results, which entails that particle production mechanisms are not tied to initial nuclear configurations.

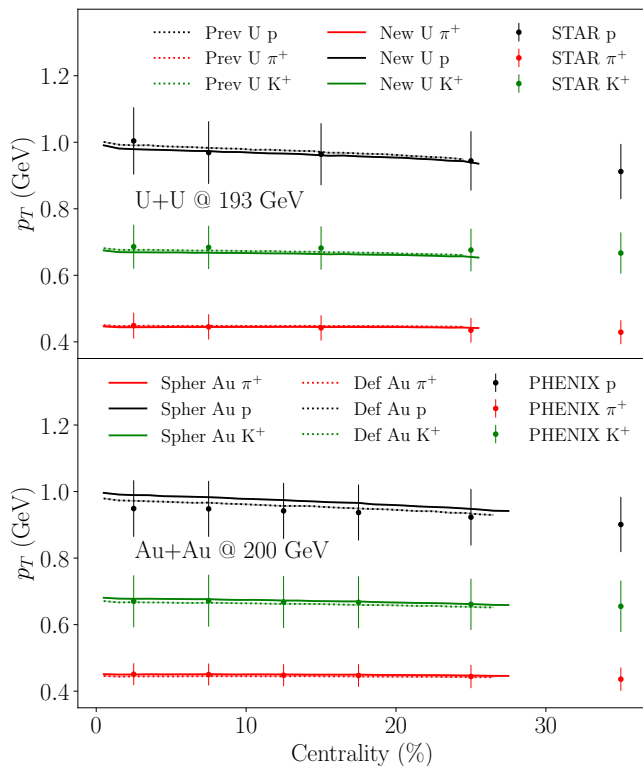


FIG. 6. Identified particle mean transverse momentum $\langle p_T \rangle$ in $|y| < 0.5$ as a function of centrality in our model. **(Top)** Two U configurations compared to results for 193 GeV U+U collisions at STAR [83]. **(Bottom)** Two Au configurations compared to results for 200 GeV Au+Au collisions at PHENIX [84].

2. Average Transverse Momentum

We now move to the average transverse momentum of identified particles. Fig. 6 shows identified particle mean transverse momentum $\langle p_T \rangle$ as a function of centrality. Here, while different configurations do still give similar results, a more clear separation can be seen. This is mostly driven by the differences in size of the various configurations. Indeed, a smaller nucleus leads to (generally) smaller overlap areas in the transverse plane at equal collision energy, which in turn leads to higher energy densities and larger transverse momenta (again, at fixed collision energy). It is important to note here that size doesn't exclusively refer to the unmodified radius R_0 listed in Tab. I, but rather to the combination of all Woods-Saxon parameters, as what we are really probing for is the shape of the overlap area between the nuclei, which is affected by all WS parameters simultaneously. The respective masses of the identified particles are responsible for the ordering. Again, as with yields, kaons, pions and protons all show excellent agreement with the experimental data. It is important to note that given our use of hydrodynamics, $\langle p_T \rangle$ puts strong constraints on the p_T spectrum, which entails that a good agreement

with $\langle p_T \rangle$ is equivalent to reproducing the spectrum [86]. Therefore, given our excellent agreement with experimental data, the shear and bulk viscosity parametrizations, along with our switching temperature T_{sw} seem appropriate.

3. Anisotropic Flow

We now shift our attention to anisotropic flow, focusing on integrated elliptic and triangular flows. Fig. 7 shows the two- and four-particle cumulants of elliptic flow ($v_2\{2\}$ and $v_2\{4\}$) as functions of charged hadron multiplicity and centrality. We see that our model reproduces both observables very well. All of these results were calculated using the typical oversampled averaging method. At smaller multiplicities (or more peripheral collisions), our model overestimates U elliptic flow. This is due to the same effect apparent in Fig. 3, namely that our peripheral centrality class may contain more peripheral events which weren't rejected by our centrality selection process. It should be emphasized that no additional adjustments of parameters were made to produce our results. It should also be noted that the Au data does not have the same overestimating feature in peripheral collisions, further proving that this is an artifact of our centrality selection process.

Looking at the two U configurations, one finds a slight (but marked) improvement going from Prev ^{238}U to New ^{238}U . The slight decrease in β_2^0 leads to a general decrease in the two-particle cumulant of elliptic flow in central ($\sim 0 - 10\%$) collisions. The four-particle cumulant, on the other hand, seems unaffected by the change, if only because the error bars are too large to draw conclusions.

The Au configurations show a marked split in central collisions, once again driven by the inclusion (and exclusion) of β_2^0 . In the most central collisions, the spherical parametrization underestimates $v_2\{2\}$ by a wide margin, leading us to conclude that ^{197}Au is deformed. While the deformed ^{197}Au configuration does mirror the experimental data well, it consistently underestimates the experimental values throughout the multiplicity and centrality ranges. This underestimation, while small, does open the door to future analyses using slightly larger values of β_2^0 and β_2^2 . Also interestingly, the four-particle cumulant shows absolutely no sensitivity to the changes in parametrization (from perfectly spherical to deformed), which, combined to similar observations for the two U configurations, indicates that this cumulant is mainly driven by either higher-order deformation parameters or fluctuations.

One may notice that our model does not reach as high in multiplicity as the experimental data does. This is because the experimental points beyond $dN_{ch}/d\eta \approx 850$ constitute ultra-ultra-central collisions. That is, they are in the top 0.01% of events registered at STAR; these experimental events are rare and would require a much larger number of runs on our part to reproduce. Nev-

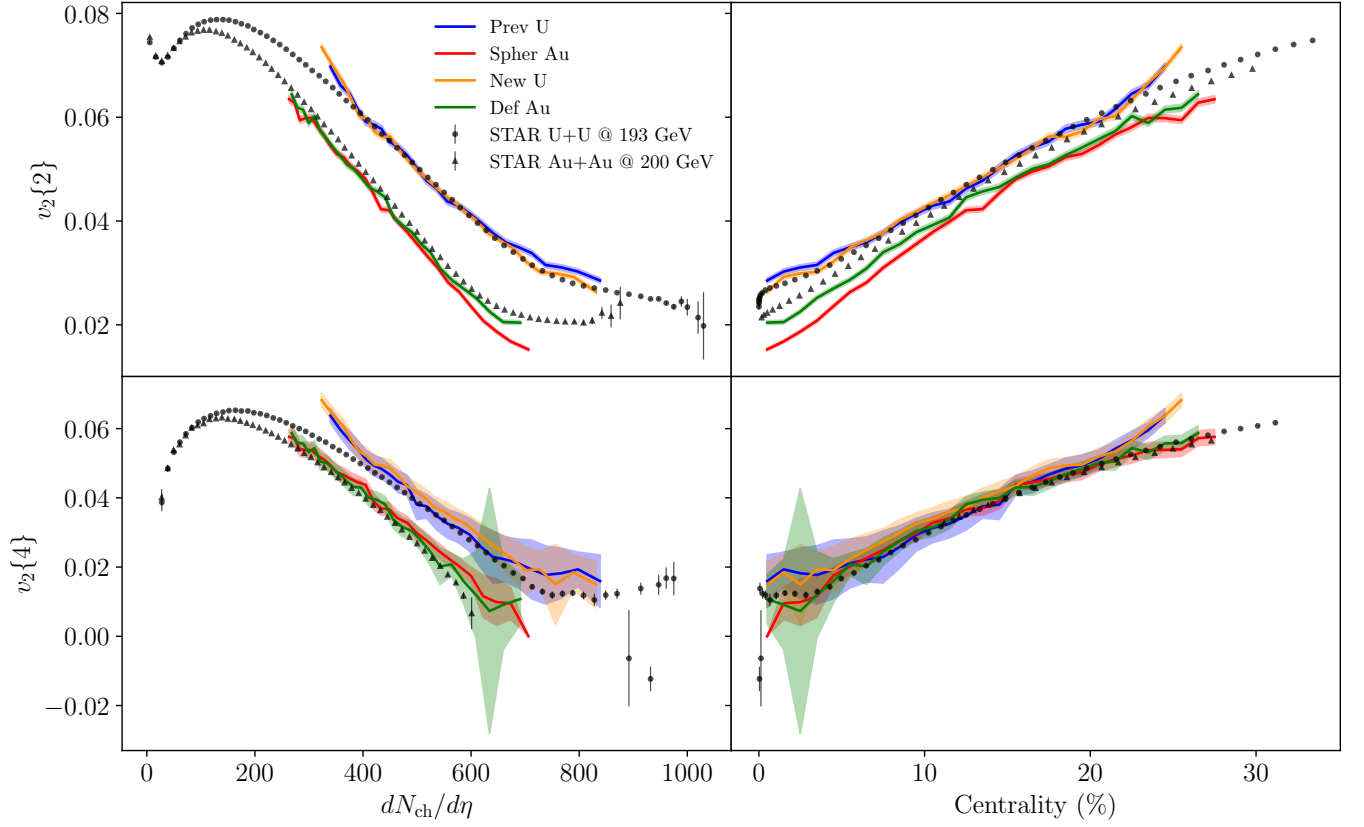


FIG. 7. Two- and four-particle cumulants of elliptic flow ($v_2\{2\}$ and $v_2\{4\}$) as functions of **(left)** charged particle multiplicity and **(right)** centrality, compared to results for 193 GeV U+U and 200 GeV Au+Au collisions at STAR [3, 85]. The shaded bands represent statistical errors.

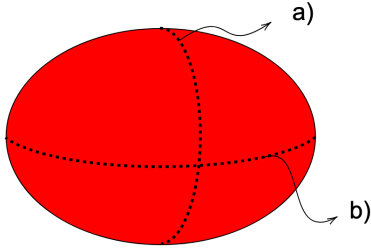


FIG. 8. Schematic representation of the asymmetry between a) the short-axis and b) the long-axis directions. In the short axis direction, the nucleus is not deformed (has constant R in WS parametrization).

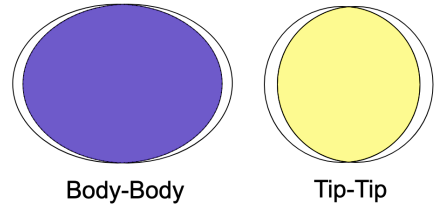


FIG. 9. Schematic representation of the difference in nuclei overlap area between body-body and tip-tip collisions. The former presents large eccentricity while the latter presents near-zero eccentricity.

ertheless, the right side panels show that, in terms of centrality, we are essentially reproducing the entire spectrum of central events.

These right-side panels also serve to compare Au and U data more accurately. We see that experimental $v_2\{2\}$'s are extremely similar throughout the centrality spectrum, except in the very central collisions (0 – 5%). There, U data shows a marked increase before coming back to Au levels between 0 – 1%. This is explained by

the considerably deformed geometry of U. In central collisions of spherically symmetric nuclei, only one overlap shape is generated in the transverse plane, namely a circle, which has small (or 0) eccentricity. This in turn leads to a small elliptic flow in the final state. In central collisions of largely deformed nuclei such as U, many different transverse cross-sections are possible. Indeed, looking at Figs. 8 and 9 we see that a nucleus travelling with its long axis parallel to the beam direction will have a circu-

lar cross-section in the transverse plane. Similarly, if its short axis is parallel to the beam direction, it will have an elliptical transverse cross-section. Therefore, in collisions of deformed nuclei with near-zero impact parameters, we can have both extremely eccentric (body-body) and circular (tip-tip) cross-sections. The body-body collisions will have a smaller energy density (due to their larger transverse overlap area) than their tip-tip counterparts, which will in turn lead to slightly smaller multiplicities. Therefore, the marked increase in $v_2\{2\}$ in 1–3% centrality is due to body-body collisions, and its sharp decrease in ultra-central (0 – 1%) collisions is due to tip-tip collisions.

These panels also serve as an indication that, while ^{197}Au may be deformed, its deformation is fairly small compared to that of ^{238}U , as the specific features described above are much less prominent for ^{197}Au than for ^{238}U . They also further support the idea that $v_2\{4\}$ is driven by fluctuations, as both the ^{197}Au and ^{238}U experimental results overlap throughout.

Fig. 10 introduces an alternative averaging method described in section III B, namely the SMASH sub-event averaging. This sub-event averaging method leads to the expression of short-range correlations which are usually suppressed by oversampled averaging. We note that, for our two U configurations, this method leads to a slight overestimation of $v_2\{2\}$ across the entire centrality range. For Au, we observe the same behavior in moving from oversampled averaging to SMASH sub-event averaging, namely a small increase in $v_2\{2\}$. In all cases, however, both methods seem rather similar, indicating that short-range correlations and fluctuations do not play a significant role in elliptic flow. As it stands, neither the oversampling averaging nor the sub-event averaging faithfully follows what takes place in a real heavy-ion collision because hydrodynamics is an inherently coarse-grained theory of ensemble-averaged quantities. As such, one should regard the results of the two different averaging procedures as a part of theoretical uncertainty ($\sim 5\%$).

Fig. 10 also sees the addition of a mixed event curve which was left out of Fig. 7 for clarity. By mixing the events, only the average effect of the collision geometry should survive, whereas the effects due to the deformation will be washed out. This is indeed what can be observed in Fig. 10: it clearly shows that deformation effects are crucial in understanding flow in U+U and Au+Au collisions.

Fig. 11 shows the two-particle cumulant of elliptic flow as a function of scaled multiplicity in two ultra-central ZDC bins: 0 – 0.125% and 0 – 1%. These events were selected based on their respective number of sampled spectator neutrons, as described in section III A. For all configurations and collision systems, the most central bin suffers from a small number of events, which in turn affects statistics. Nevertheless, the scale of the experimental data is reproduced. The Spher ^{197}Au configuration underestimates the elliptic flow in both bins, which is expected considering Fig. 7, namely that this configura-

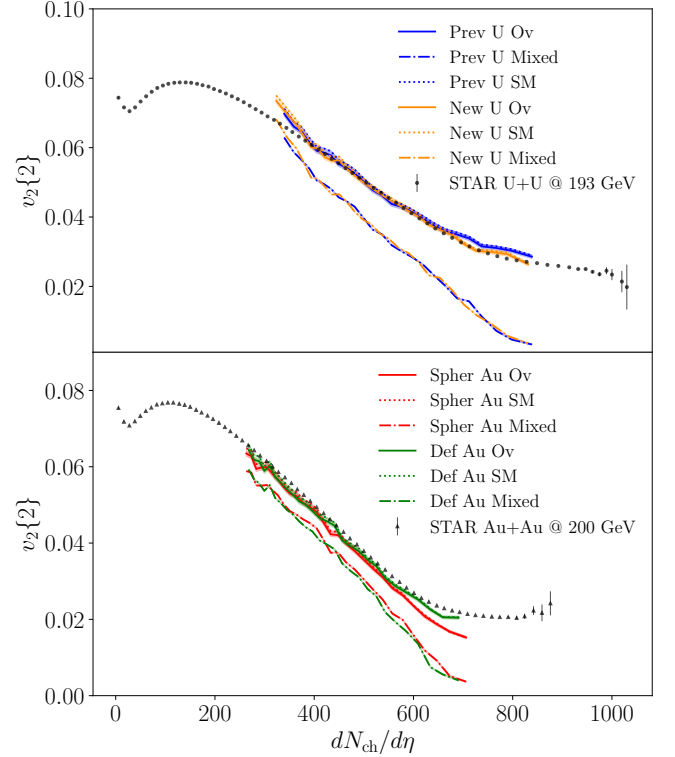


FIG. 10. Two-particle cumulant of elliptic flow ($v_2\{2\}$) as functions of charged particle multiplicity for our two systems and four configurations, emphasizing the addition of Mixed Event and SMASH sub-event average curves. **(Top)** Two U configurations compared to results for 193 GeV U+U collisions at STAR [83]. **(Bottom)** Two Au configurations compared to results for 200 GeV Au+Au collisions at STAR [85]. Here, SM stands for SMASH sub-event average while Ov stands for oversampled average.

tion was inappropriate for central collisions of Au nuclei. In the broader ultra-central bin, our model reproduces the general shape and trend of experimental data. For our two U configurations, we find New ^{238}U to reproduce the experimental data more faithfully, in line with what we’ve been able to conclude from Fig. 7. The Def ^{197}Au configuration performs decently in this broader centrality window. However, it considerably underestimates elliptic flow at smaller multiplicities. This is most probably due to relatively low statistics, but will require further investigation.

Fig. 12 shows the two-particle cumulant of triangular flow $v_3\{2\}$ as a function of charged particle multiplicity, which is a fluctuation-driven observable. Looking at Fig. 12, we see that experimental data for U and Au are practically overlapping in central collisions, confirming that initial global geometry plays little role in this observable. Our model underestimates triangular flow across our chosen range, collision systems and configurations, which indicates that it underestimates initial state fluctuations. This could potentially be mended by the addition of sub-nucleonic degrees of freedom (i.e. valence

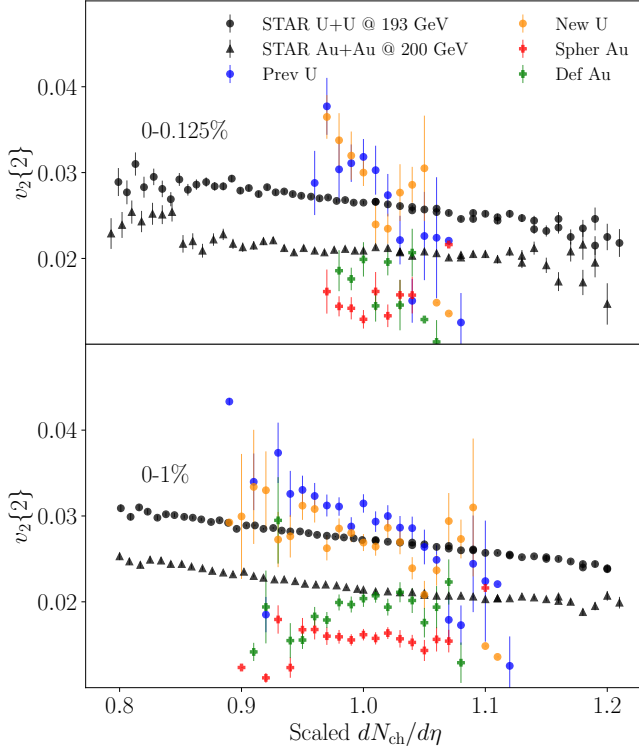


FIG. 11. Two-particle cumulant of elliptic flow ($v_2\{2\}$) as functions of scaled charged particle multiplicity for (**top**) 0 – 0.125% and (**bottom**) 0 – 1% most central events, compared to results for 193 GeV U+U and 200 GeV Au+Au collisions at STAR [3].

quark configurations) in our initial construction of the nuclear thickness function $T_A(\mathbf{x})$, such as those described in [87]. Interestingly, we also see that our SMASH sub-event average curves are consistently lower than their oversampled average counterparts. This result implies that our current exclusion of sub-nucleonic degrees of freedom leads to short-range fluctuations being noticeably smaller than longer-range ones.

Finally, we turn to Fig. 13, which shows the ratio of $v_2\{2\}^2$ between U+U at 193 GeV and Au+Au at 200 GeV, i.e.

$$r_{\text{Au,U}}(v_2\{2\}^2) = \frac{v_2\{2\}_{\text{U+U}}^2}{v_2\{2\}_{\text{Au+Au}}^2} \quad (51)$$

We have opted to include only one such ratio, as Fig. 7 is sufficiently descriptive to enable us to select the most appropriate parametrizations for this calculation, namely New ^{238}U and Def ^{197}Au (as parametrized in Tab. I), as those are obviously closest to the experimental data. The figure shows that our model overestimates the ratio throughout the considered centrality range. While the ratio is fairly close to the experimental data, our model's slight underestimation of the Au elliptic flow, discussed previously, leads to an overestimation of the ratio. It is

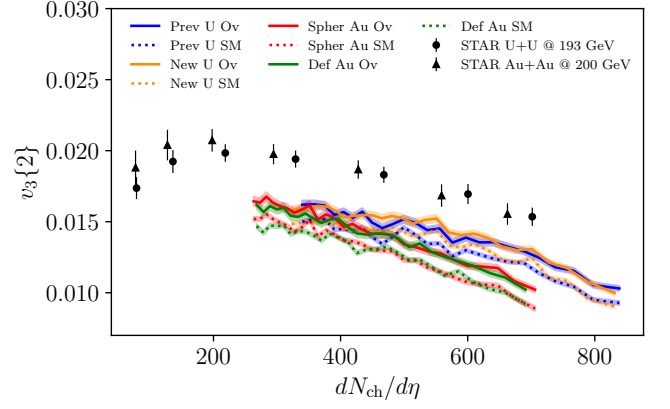


FIG. 12. Two-particle cumulant of triangular flow ($v_3\{2\}$) as a function of charged particle multiplicity, compared to results for 193 GeV U+U and 200 GeV Au+Au collisions at STAR [4]. Here, *SM* stands for SMASH sub-event average while *Ov* stands for oversampled average.

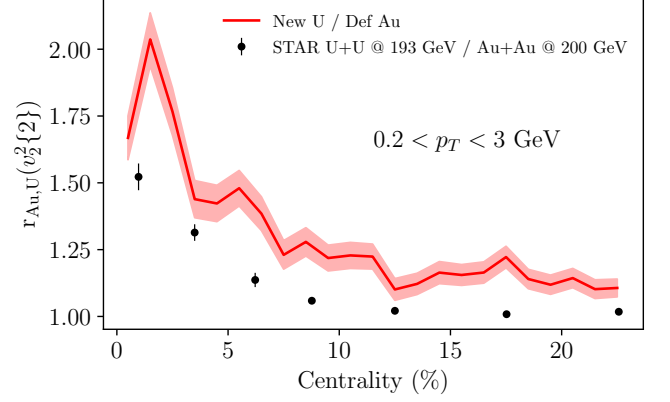


FIG. 13. Ratio of mean squared elliptic flow $v_2\{2\}^2$ for our two best-fit parametrizations, New U and Def Au (c.f. Tab. I), compared to experimental results for 193 GeV U+U and 200 GeV Au+Au collisions at STAR [88].

however important to reiterate that our model does very well at reproducing the two-particle cumulant of elliptic flow for both systems, especially considering that only a single calibration was undertaken. Furthermore, our calculations between 0 – 1% and 3 – 4% fall close to the experimental values, which happen to be the most sensitive points to initial geometry. Given the excellent agreement between our $v_2\{2\}$ calculation and experimental data, this result points to 2 possible avenues for improvements. Firstly, it seems like a small increase in $\beta_{2,\text{Au}}^i$ would help the ratio fall within the experimental data over the entire range. Secondly, an individually calibrated run for Au may help, although the effects of such a calibration on elliptic flow would be small compared to changes in its quadrupole moment.

B. Predictions

We now move on to predictions of our model for multi-particle correlations and transverse-momentum-flow correlations for $\sqrt{s_{NN}} = 193$ GeV U+U collisions.

1. Differential flow

In this section, our predictions for U+U collisions will be contextualized using Au+Au experimental results and simulation data.

Fig. 14 introduces our predictions for the differen-

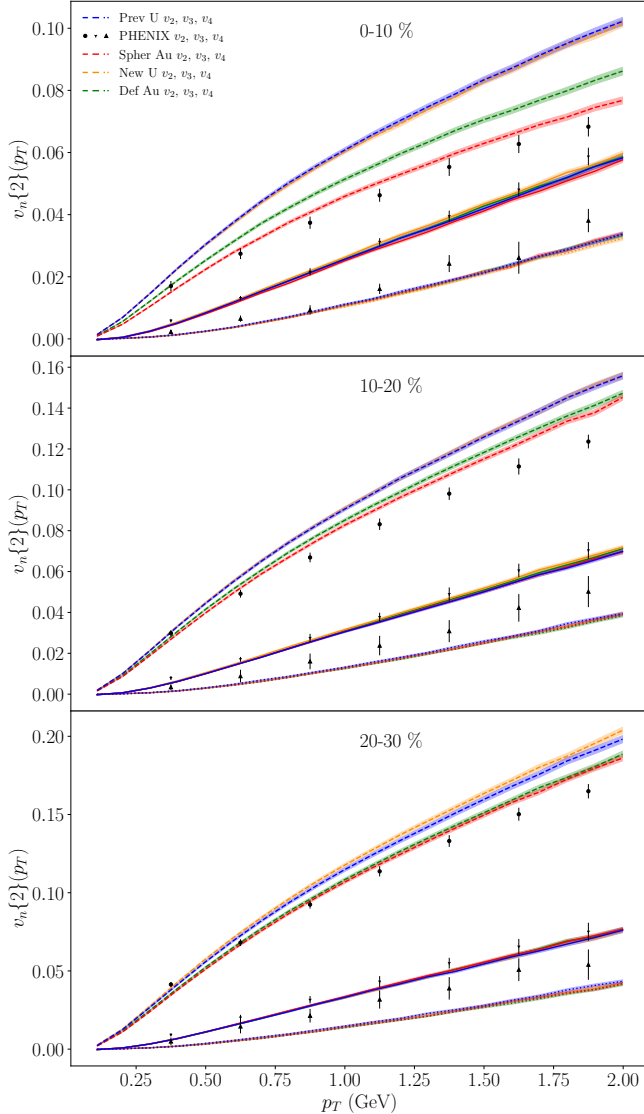


FIG. 14. Model predictions of charged hadron differential anisotropic flow coefficients $v_2\{2\}$, $v_3\{2\}$ and $v_4\{2\}$ as functions of transverse momentum p_T for various centrality classes for U+U, compared to experimental results from PHENIX [16] and model calculations for 200 GeV Au+Au collisions.

tial v_n for U+U at $\sqrt{s_{NN}} = 193$ GeV compared to experimental results and our simulations for Au+Au at $\sqrt{s_{NN}} = 200$ GeV. We find that our model's calculations of $v_3\{2\}(p_T)$ for U+U and Au+Au is similar to the Au+Au event-plane v_3 data from PHENIX [16]². This is expected because v_3 depends mainly on local fluctuations which are similar in the two systems, and are unaffected by initial configurations.

Differential elliptic flow (v_2) for U+U is larger across all centrality classes than v_2 for Au+Au, independent of configurations. The differences do, however, get smaller as we move towards more peripheral regions. For the 0–10% centrality class, this is consistent with the deformation effects discussed in section IV A 3: we expect the elliptic flow to be enhanced in this region of the centrality spectrum because of the elliptic shape of ^{238}U nuclei. The two Au configurations overestimate differential v_2 for $p_T \geq 0.5$ GeV. While it may seem like cause for concern, it is important to remember that most produced particles have transverse momenta less than 1 GeV, meaning that higher p_T contributions to the integrated elliptic flow are relatively small. Nevertheless, this high- p_T discrepancy is worth looking into, as it may point towards inadequacies within our hydrodynamics modelling.

In the 10–20% and 20–30% classes, the differences are smaller and are themselves consistent with elliptic flow being noticeably larger for U+U collisions compared to Au+Au throughout the collision spectrum, as evidenced in Fig. 7. The two configurations from both systems end up with overlapping v_2 lines, which further confirms that specific nuclear structure does not play an important role beyond central collisions. As for v_4 , both collision systems underestimate this observable in peripheral (10–30%) collisions. In central (0–10%) collisions, both collision systems overlap with themselves and the experimental data. Therefore, our model predicts that v_4 for U+U collisions at 193 GeV should be similar (if not equal) to that of Au+Au collisions at 200 GeV.

Finally, Fig. 15 shows differential elliptic flow for identified particles from our model and from Au+Au collisions at STAR [17]. This figure only includes two configurations (one for each system) for clarity, given that general conclusions given the ordering of the elliptic flow of the different configurations can already be extracted from Fig. 14. Our Au calculations reproduce the experimental data well across all four centrality ranges. Our model, as seen previously, predicts a larger differential elliptic flow for U than for Au. In the ultra-central regions (0–5% & 5–10%), the effect is clear and crosses hadronic lines. However, in the more peripheral regions (10–20% & 20–30%), this difference becomes much smaller, and varies considerably from one hadron to another; our model's predictions for anti-protons is similar to both Au experimental data and our model's calculation.

² The PHENIX data here does not use the scalar-product method.

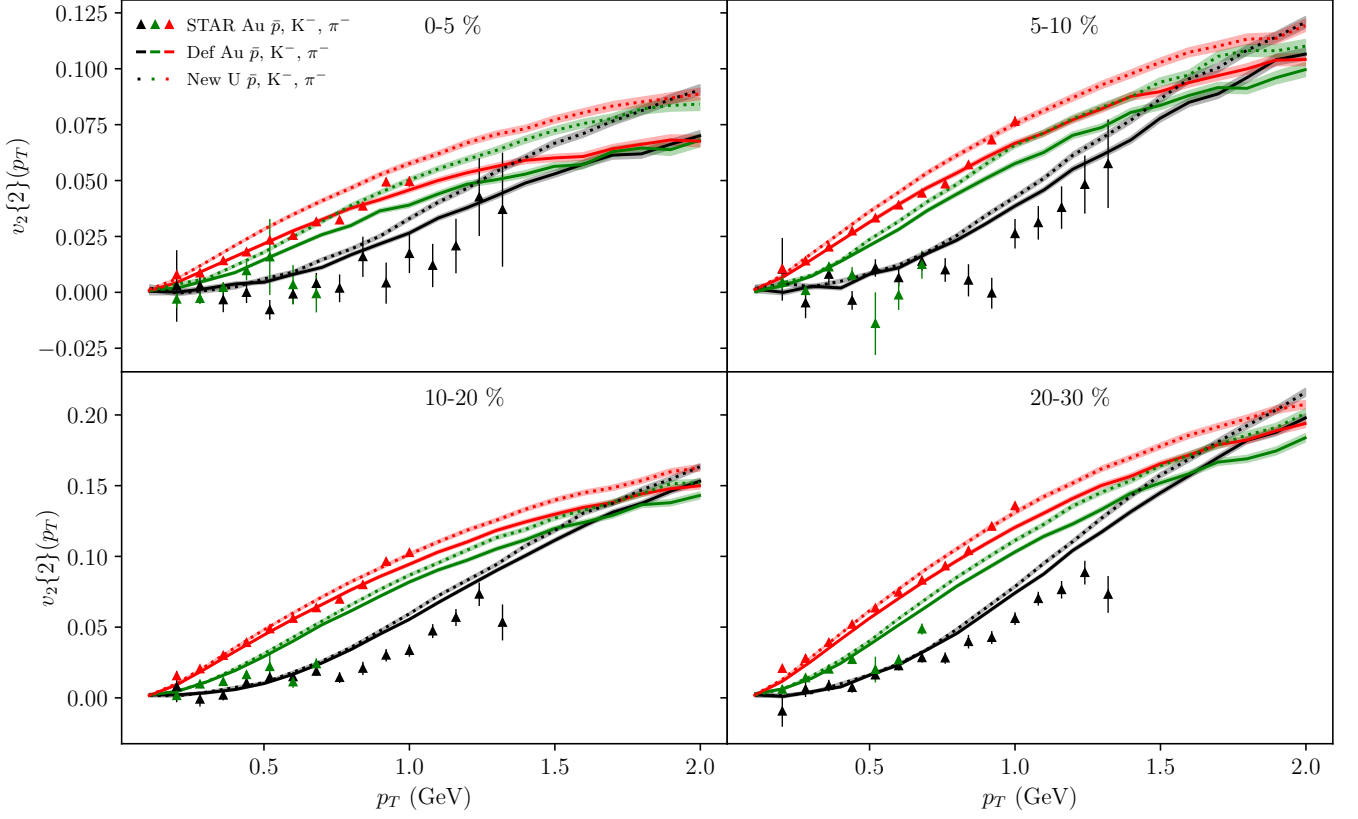


FIG. 15. Model prediction of identified particle differential elliptic flow coefficients $v_2\{2\}$ as a function of transverse momentum p_T for various centrality classes for U+U at 193 GeV, compared to experimental results at STAR [17] and model calculations for 200 GeV Au+Au collisions.

tion. Higher- p_T differential flow seems to converge consistently across all identified particles.

The final two results subsections will contain predictions of our model compared to experimental data. This may seem like a contradiction, but our calculations were done and published to the arXiv before the publication of Ref. [88], as evidenced by the first version of this manuscript [89]. As such, the following observables figure as predictions of our model, and no further calibration was undertaken following the publication of Ref. [88].

2. Multi-particle Momentum Correlations

Multi-particle correlations, when compared to experimental data and combined with primary observables such as elliptic flow, can help constrain ^{238}U 's, ^{197}Au 's and other nuclei's deformation parameters and can allow for further analysis using various sets of deformation parameters [88, 90].

In the top panels of Fig. 16, we show the 2-particle p_T correlator compared to experimental data from STAR [88]. In both plots, we have included a mixed event curve to ensure that no underlying p_T correlations exist - its position on the plot confirms this. A sizeable

difference exists between our oversampled event average and SMASH sub-event average curves, which are diametrically opposed with respect to our mixed event curve. This indicates that the inclusion (or exclusion) of short-range correlations are a key determinant of the behaviour of this observable across collision systems. Our SMASH sub-event average curves match available experimental data rather well, with the Prev ^{238}U and Def ^{197}Au configurations as best matches. This shows that, contrarily to other primary observables like the elliptic flow where oversampled averaging led to best results, the 2-particle p_T correlator depends on taking the SMASH sub-event average in order to reproduce experimental data. This implies that short-range correlations play a large role in this experimental observable. It is also of interest that the strength of the correlations (or anti-correlations) differs between the two collision systems. This difference is mainly driven by deformity, as is evidenced by the fact that a clear ordering exists between our configurations, going from least deformed (Spher ^{197}Au) to most deformed (Prev ^{238}U). Indeed, the experimental U $\langle\delta p_T\delta p_T\rangle$ curve increases between 0 and 2% centrality, while the Au curve does not. Because ultra-central collisions of deformed nuclei have a wider variety of geometrical configurations, correlations of dynamical p_T fluctu-

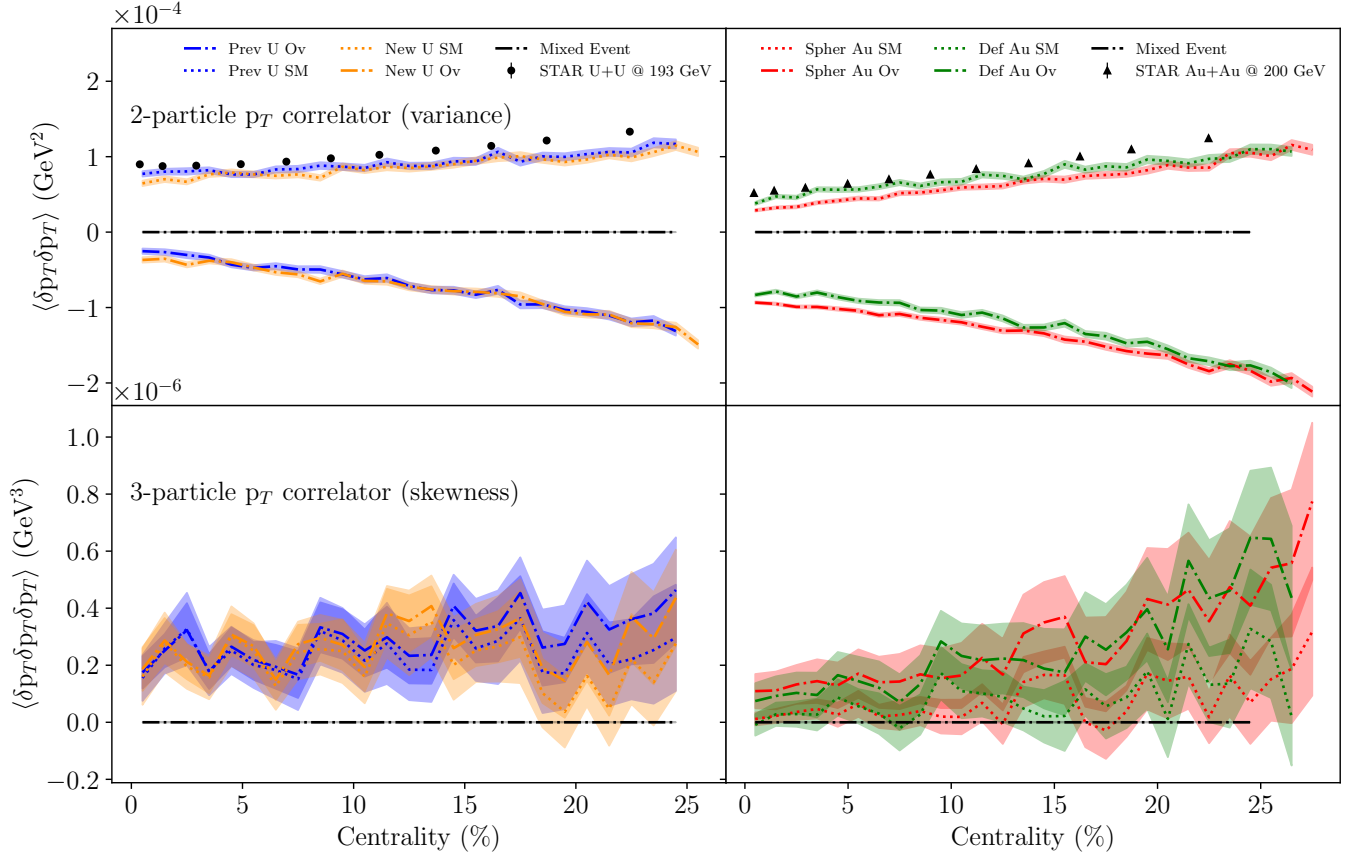


FIG. 16. **(top)** 2- and **(bottom)** 3-particle momentum correlators as functions of centrality, with $0.2 \text{ GeV} \leq p_T \leq 3.0 \text{ GeV}$, for **(left)** U+U at 193 GeV and **(right)** Au+Au at 200 GeV, compared to experimental results at STAR [88]. Here, *SM* stands for SMASH sub-event average while *Ov* stands for oversampled average.

ations increase as well: the number of pairs of particles with p_T considerably deviating from the centrality class $\langle p_T \rangle$ swells thanks to the distinct groups (body-body and tip-tip) of collision geometries present in said centrality class.

The bottom panels of Fig. 16 shows the 3-particle p_T correlator. In contrast to the upper panel, both curves are extremely similar, with the oversampled average only slightly larger than the SMASH sub-event averaging values. The oversampled averaging technique gives out larger correlations, which serve as a further contrast to the behaviour of the curves in the upper panel. 3-particle correlations are slightly larger, in general, for U compared to Au, especially in central collisions. Interestingly, the SMASH sub-event averaging and oversampled averaging curves diverge in peripheral Au collisions; this does not, however, occur in our U calculations. Once again, the mixed event curve is included to ensure that no implicit correlations exist for this observable.

Fig. 17 shows the ratio of the 2-particle p_T correlator, defined as

$$r_{\text{Au,U}}(\langle \delta p_T \delta p_T \rangle) = \frac{\langle \delta p_T \delta p_T \rangle_{\text{U}}}{\langle \delta p_T \delta p_T \rangle_{\text{Au}}} \quad (52)$$

Here, only the SMASH sub-event averaged correlator values were used, as they were an obvious match for the available experimental results. The best ratios are obtained using the Def ^{197}Au parametrization in the denominator, with that using the New ^{238}U parametrization in the numerator being a slightly better match for experimental data than Prev ^{238}U . This is in contrast to what had been observed in Fig. 16's top-left panel, where Prev ^{238}U seemed to have been better at describing the experimental results. This shows one of intrinsic cons of using ratios as observables: this new observable is really two independent observables wrapped into one, and two underestimates can lead to the ratio being spot-on.

It is however understood that observables measured in one collision system are largely shaped by the underlying hydrodynamic properties of the QGP. Taking ratios of observables can, in some cases, help ease the existing tension, by giving a composite observable which is essentially independent of the hydrodynamic phase [88].

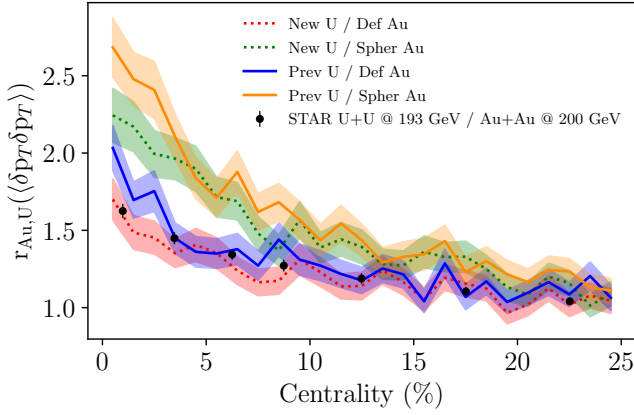


FIG. 17. Ratio of the 2-particle p_T correlator for all U and Au parametrizations, compared to experimental results for U+U at 193 GeV and Au+Au at 200 GeV collisions at STAR [88]

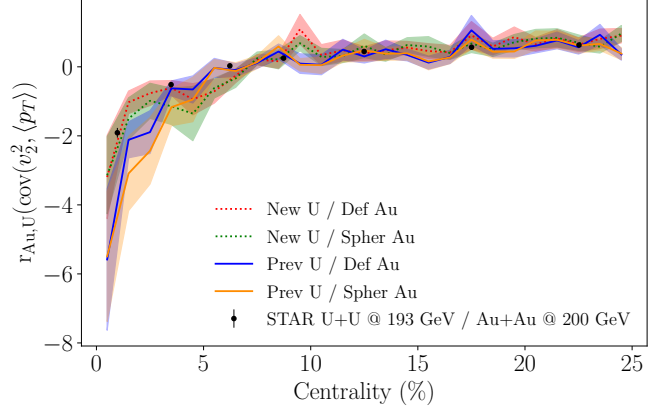


FIG. 19. Ratio of the elliptic-flow-momentum correlations for all U and Au parametrizations, compared to experimental results for U+U at 193 GeV and Au+Au at 200 GeV collisions at STAR [88]

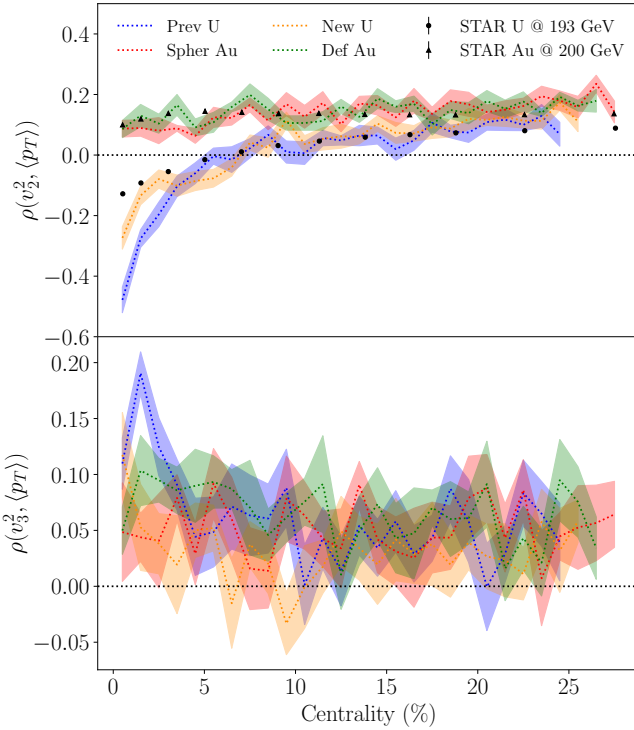


FIG. 18. **(top)** Elliptic and **(bottom)** triangular flow and $\langle p_T \rangle$ correlations as functions of centrality for U+U at 193 GeV and Au+Au at 200 GeV, compared to experimental results from STAR [88].

3. Transverse-Momentum-Flow Correlation

We end our results section with plots showing predictions for the correlations between integrated anisotropic flow and mean transverse momentum. This observable has garnered interest as a tell-tale sign of deformation [81].

Fig. 18 only includes oversampled average calculations,

as using the SMASH sub-event averaging method simply leads us to carry over the overestimation of $v_2\{2\}$ into the correlator. The mixed event curve could not be included in this plot as it is undefined across our centrality interval. Indeed, referring to Eq.(48), the correlator $\rho(v_n^2, \langle p_T \rangle)$ requires a division by $\langle \delta p_T \delta p_T \rangle$ which is evenly 0 across our centrality interval, as evidenced by Fig. 16. Triangular-flow-momentum (bottom panel) correlations seem to be dominated by fluctuations, with the only real clear trend being that the correlator remains positive throughout the centrality range and across both collision systems and nuclear parametrizations. No experimental data was available for this observable. Elliptic-flow-momentum correlations, on the other hand, show clear differences when moving from one collision system to the other. Both collision systems achieve excellent agreement with available experimental data. Indeed, Au correlations are positive throughout the centrality range; they show a slight, consistent increase as we move from central to peripheral collisions. The small quadrupole deformation of Def ^{197}Au has no tangible effect on the observable. U correlations, on the other hand, behave considerably differently. While the effects of changing the deformation parameters between runs are as subtle as for Au, a clear cross-over from correlation to anti-correlation occurs at around the 7% centrality mark in both configurations, as well as in the experimental data.

In central collisions of (near-)spherical nuclei [8, 9], we expect and observe a dip in the correlator due to the correlation between the inverse of the transverse overlap area (larger mean p_T) and initial state eccentricity ϵ_2 (which gets smaller in more central collisions). However, no anti-correlation is observed. Our model predicted that, for U+U collisions, an anti-correlation should be observed in central collisions; the experimental data shows that this prediction turned out true. We can make sense of this prediction and experimental result by using the correla-

tion between inverse overlap area and eccentricity. Indeed, tip-tip collisions will generate relatively small overlap areas that are high in energy density (leading to high $\langle p_T \rangle$) while generating almost no eccentricity and therefore, elliptic flow. Therefore, when contrasted with other events (such as body-body events) in a given centrality class, the correlator finds that $\langle p_T \rangle$ and $v_2\{2\}$ are anti-correlated, as events in these classes having lower $\langle p_T \rangle$ and higher eccentricities contrast other events in the same centrality class having larger $\langle p_T \rangle$ and smaller eccentricities.

Finally, as with $v_2\{2\}$ and $\langle \delta p_T \delta p_T \rangle$, Fig. 19 shows the ratio of covariances of $v_2\{2\}$ and p_T of our two collision systems, i.e.

$$r_{\text{Au,U}}(\text{cov}(v_2\{2\}^2, \langle p_T \rangle)) = \frac{\text{cov}(v_2\{2\}^2, \langle p_T \rangle)_{\text{U}}}{\text{cov}(v_2\{2\}^2, \langle p_T \rangle)_{\text{Au}}} \quad (53)$$

where $\text{cov}(v_2\{2\}^2, \langle p_T \rangle)$ is defined in Eq. (49). The covariances were kept instead of the full correlation in order to properly reflect the experimental data found in [88].

All ratios perform well in more peripheral ($> 10\%$ centrality) collisions. In central collisions, ratios including the Prev ^{238}U configurations fall noticeably lower than the experimental results. While both ratios including the New ^{238}U parametrization perform well, the experimental data shows a marked preference for the New ^{238}U / Def ^{197}Au ratio. Therefore, while Fig. 18 could not truly separate between the two Au parametrizations, taking the ratio of the covariances has provided additional evidence that a deformed Au parametrization is more appropriate (and, therefore, that Au is indeed a deformed nucleus).

V. SUMMARY AND CONCLUSION

We have presented a detailed synthesis of our multi-phase model consisting of IP-Glasma initial state, MUSIC viscous relativistic hydrodynamics, and iS3D + SMASH particle sampling and transport, and have shown its results for a wide variety of observables for U+U collisions at $\sqrt{s_{NN}} = 193$ GeV and Au+Au at $\sqrt{s_{NN}} = 200$ GeV. The purpose of this work is to describe the published data and to present timely predictions for observables specifically relevant to deformed nuclei.

Our model shows good agreement across all available experimental data for charged hadron multiplicity, identified particle yields and integrated anisotropic flow. The underestimation of the $v_3\{2\}$ by about 15% could also be an opportunity to further study the effects of sub-nucleonic fluctuations.

All-in-all, however, our model performed very well against a limited set of experimental data and reproducing Au+Au experimental data it had not been expressly calibrated to reproduce. Particularly impressive was matching new experimental data ($\rho(v_2^2, \langle p_T \rangle), \langle \delta p_T \delta p_T \rangle$) that our model had initially output as predictions.

Our model's physics-based approach allowed us to make predictions regarding flow and bulk observables and interpret them phenomenologically. Furthermore, we were able to use it to test different averaging techniques and determine their effects on observables. In the case of 2-particle momentum correlations, these two methods led to widely different values. This clear difference presents itself as a golden opportunity to determine which types of fluctuations and correlations (either local or global) dominate the p_T spectrum in U+U collisions at $\sqrt{s_{NN}} = 193$ GeV. This prediction could also be of use in constraining ^{238}U deformation parameters, as momentum correlators are sensitive to nuclear deformation [90]. Another compelling prediction of our model was that of a definite cross-over towards anti-correlation of $v_2\{2\}$ and $\langle p_T \rangle$ in central collisions, at about the 7% mark. This is in stark contrast to reported correlations of spherically symmetric nuclei [9], our calculations for Au+Au at $\sqrt{s_{NN}} = 193$ GeV, as well as results obtained in other works using our model [23]. If such an anti-correlation is detected in future experimental work, it would validate our phenomenological reasoning as well as our model. Finally, our predictions regarding the differential flow for charged hadrons and identified particles were consistent across centrality classes when compared to data for Au+Au collisions at RHIC. Indeed, the observables acted as expected given available integrated flow observables. We emphasize that even though the experimental data are included for the correlation observables, our calculations were done before the publication of Ref. [88] as the initial version of this manuscript showed [89].

Our work here sets the stage for further calculations regarding deformed nuclei, be it ^{238}U specifically or others, such as ^{129}Xe [91]. Indeed, while our current work seems to suggest a good understanding of the structure of ^{238}U and ^{197}Au , many details remain to be explored. As our models become better at describing heavy-ion collisions, we must prove increasingly diligent regarding the nuclear parametrizations we use. While our best-performing ^{238}U and ^{197}Au parametrizations were satisfactory, more details are certainly required to represent physical reality adequately; we think here of different and more recent nuclear parametrization paradigms, such as Nuclear Density Functional Theory (NDFT) [92], which provide deeper and more physical constraints on nucleon positions and correlations. In the end, we would want to use sensitive observables available experimentally to constrain nuclear deformation, allowing us to further perfect our state-of-the-art simulations and provide a deeper understanding of strongly interacting matter at various stages.

ACKNOWLEDGMENTS

We would like to acknowledge the support of the entirety of our research group at McGill University. We also

acknowledge insightful conversations with R. Modarresi Yazdi, M. Heffernan, S. McDonald, S. Shi, B. Schenke C. Shen, J. Jia and C. Zhang. This work was funded by the Natural Sciences and Engineering Research Council of Canada (NSERC) [SAPIN-2018-00024 ; SAPIN-2020-00048]. Computations were made on the Béluga super-computer system from McGill University, managed by

Calcul Québec (calculquebec.ca) and Digital Research Alliance of Canada (alliancecan.ca). The operation of this supercomputer is funded by the Canada Foundation for Innovation (CFI), Ministère de l'Économie, des Sciences et de l'Innovation du Québec (MESI) and le Fonds de recherche du Québec - Nature et technologies (FRQ-NT).

-
- [1] H. De Vries, C. W. De Jager, and C. De Vries, Nuclear charge-density-distribution parameters from elastic electron scattering, *At. Data Nucl. Data Tables*; (United States) **36**, [10.1016/0092-640X\(87\)90013-1](https://doi.org/10.1016/0092-640X(87)90013-1) (1987).
 - [2] W. Ryssens, G. Giacalone, B. Schenke, and C. Shen, Evidence of hexadecapole deformation in uranium-238 at the relativistic heavy ion collider, *Physical Review Letters* **130**, [10.1103/physrevlett.130.212302](https://doi.org/10.1103/physrevlett.130.212302) (2023).
 - [3] L. Adamczyk, J. Adkins, G. Agakishiev, M. Aggarwal, Z. Ahammed, I. Alekseev, J. Alford, A. Aparin, D. Arkhipkin, E. Aschenauer, *et al.*, Azimuthal Anisotropy in U+U and Au+Au Collisions at RHIC, *Physical Review Letters* **115**, [10.1103/physrevlett.115.222301](https://doi.org/10.1103/physrevlett.115.222301) (2015).
 - [4] J. Adam, L. Adamczyk, *et al.*, Azimuthal harmonics in small and large collision systems at RHIC top energies, *Physical Review Letters* **122**, [10.1103/physrevlett.122.172301](https://doi.org/10.1103/physrevlett.122.172301) (2019).
 - [5] W. Busza, K. Rajagopal, and W. van der Schee, Heavy ion collisions: The big picture and the big questions, *Annual Review of Nuclear and Particle Science* **68**, 339 (2018).
 - [6] R. Pasechnik and M. Šumbera, Phenomenological review on quark–gluon plasma: Concepts vs. observations, *Universe* **3**, 7 (2017).
 - [7] E. V. Shuryak, High energy collisions of strongly deformed nuclei: An old idea with a new twist, *Phys. Rev. C* **61**, 034905 (2000).
 - [8] B. Schenke, C. Shen, and D. Teaney, Transverse momentum fluctuations and their correlation with elliptic flow in nuclear collisions, *Physical Review C* **102**, [10.1103/physrevc.102.034905](https://doi.org/10.1103/physrevc.102.034905) (2020).
 - [9] G. Aad, B. Abbott, D. Abbott, A. Abed Abud, K. Abeling, *et al.*, Measurement of flow harmonics correlations with mean transverse momentum in Pb-Pb and p-Pb collisions at 5.02 TeV with the ATLAS detector, *The European Physical Journal C* **79**, [10.1140/epjc/s10052-019-7489-6](https://doi.org/10.1140/epjc/s10052-019-7489-6) (2019).
 - [10] U. Heinz and A. Kuhlman, Anisotropic flow and jet quenching in ultrarelativistic U+U collisions, *Physical Review Letters* **94**, [10.1103/physrevlett.94.132301](https://doi.org/10.1103/physrevlett.94.132301) (2005).
 - [11] G. Giacalone, J. Jia, and C. Zhang, Impact of nuclear deformation on relativistic heavy-ion collisions: Assessing consistency in nuclear physics across energy scales, *Physical Review Letters* **127**, 242301 (2021).
 - [12] J. Jia, Shape of atomic nuclei in heavy ion collisions, *Physical Review C* **105**, 014905 (2022).
 - [13] B. Bally, M. Bender, G. Giacalone, and V. Somà, Evidence of the triaxial structure of Xe 129 at the large hadron collider, *Physical Review Letters* **128**, 082301 (2022).
 - [14] J. Adam *et al.*, Centrality dependence of the charged-particle multiplicity density at midrapidity in Pb-Pb collisions at 5.02 TeV, *Physical Review Letters* **116**, [10.1103/physrevlett.116.222302](https://doi.org/10.1103/physrevlett.116.222302) (2016).
 - [15] S. Acharya *et al.*, Production of charged pions, kaons, and (anti-)protons in Pb-Pb and inelastic pp collisions at 5.02 TeV, *Physical Review C* **101**, [10.1103/physrevc.101.044907](https://doi.org/10.1103/physrevc.101.044907) (2020).
 - [16] A. Adare *et al.*, Measurements of higher order flow harmonics in Au+Au collisions at 200 GeV, *Physical Review Letters* **107**, [10.1103/physrevlett.107.252301](https://doi.org/10.1103/physrevlett.107.252301) (2011).
 - [17] J. Adams *et al.*, Azimuthal anisotropy in Au+Au collisions at 200 GeV, *Physical Review C* **72**, [10.1103/physrevc.72.014904](https://doi.org/10.1103/physrevc.72.014904) (2005).
 - [18] F. Gelis, E. Iancu, J. Jalilian-Marian, and R. Venugopalan, The color glass condensate, *Annual Review of Nuclear and Particle Science* **60**, 463 (2010).
 - [19] E. Iancu and R. Venugopalan, The Color Glass Condensate and high energy scattering in QCD, *Quark-Gluon Plasma 3*, 249 (2004).
 - [20] C. Gale, S. Jeon, B. Schenke, P. Tribedy, and R. Venugopalan, Event-by-event anisotropic flow in heavy-ion collisions from combined Yang-Mills and viscous fluid dynamics, *Phys. Rev. Lett.* **110**, 012302 (2013), [arXiv:1209.6330 \[nucl-th\]](https://arxiv.org/abs/1209.6330).
 - [21] C. Gale, S. Jeon, and B. Schenke, Hydrodynamic Modeling of Heavy-Ion Collisions, *Int. J. Mod. Phys. A* **28**, 1340011 (2013).
 - [22] B. Schenke, C. Shen, and P. Tribedy, Running the gamut of high energy nuclear collisions, *Physical Review C* **102**, [10.1103/physrevc.102.044905](https://doi.org/10.1103/physrevc.102.044905) (2020).
 - [23] M. R. Heffernan, C. Gale, S. Jeon, and J.-F. Paquet, Bayesian quantification of strongly-interacting matter with color glass condensate initial conditions (2023), [arXiv:2302.09478 \[nucl-th\]](https://arxiv.org/abs/2302.09478).
 - [24] S. McDonald, C. Shen, F. Fillion-Gourdeau, S. Jeon, and C. Gale, Hydrodynamic predictions for Pb+Pb collisions at 5.02 TeV, *Physical Review C* **95**, [10.1103/physrevc.95.064913](https://doi.org/10.1103/physrevc.95.064913) (2017).
 - [25] M. R. Heffernan, C. Gale, S. Jeon, and J.-F. Paquet, Early-times yang-mills dynamics and the characterization of strongly interacting matter with statistical learning (2023), [arXiv:2306.09619 \[nucl-th\]](https://arxiv.org/abs/2306.09619).
 - [26] S. McDonald, S. Jeon, and C. Gale, The 3+1D initialization and evolution of the Glasma (2023), [arXiv:2306.04896 \[hep-ph\]](https://arxiv.org/abs/2306.04896).
 - [27] B. Schenke, S. Jeon, and C. Gale, (3+1)D hydrodynamic simulation of relativistic heavy-ion collisions, *Physical Review C* **82**, [10.1103/physrevc.82.014903](https://doi.org/10.1103/physrevc.82.014903) (2010).
 - [28] S. Ryu, J.-F. Paquet, C. Shen, G.-S. Denicol, B. Schenke, S. Jeon, and C. Gale, Importance of the Bulk Viscosity of QCD in Ultrarelativistic Heavy-Ion Collisions, *Physi-*

- cal Review Letters **115**, [10.1103/physrevlett.115.132301](https://doi.org/10.1103/physrevlett.115.132301) (2015).
- [29] M. McNelis, D. Everett, and U. Heinz, Particlization in fluid dynamical simulations of heavy-ion collisions: The iS3D module (2020), [arXiv:1912.08271 \[nucl-th\]](https://arxiv.org/abs/1912.08271).
- [30] J. Weil, V. Steinberg, J. Staudenmaier, L. G. Pang, D. Oliinchenko, J. Mohs, M. Kretz, T. Kehrenberg, A. Goldschmidt, B. Bäuchle, J. Auvinen, M. Attems, and H. Petersen, Particle production and equilibrium properties within a new hadron transport approach for heavy-ion collisions, *Physical Review C* **94**, [10.1103/physrevc.94.054905](https://doi.org/10.1103/physrevc.94.054905) (2016).
- [31] R. Venugopalan and M. Prakash, Flow effects on transverse momentum spectra in ultrarelativistic nuclear collisions, *Phys. Rev. C* **41**, 221 (1990).
- [32] J. Sollfrank, P. Huovinen, M. Kataja, P. V. Ruuskanen, M. Prakash, and R. Venugopalan, Hydrodynamical description of 200-A/GeV/c S + Au collisions: Hadron and electromagnetic spectra, *Phys. Rev. C* **55**, 392 (1997), [arXiv:nucl-th/9607029](https://arxiv.org/abs/nucl-th/9607029).
- [33] P. F. Kolb, J. Sollfrank, and U. W. Heinz, Anisotropic flow from AGS to LHC energies, *Phys. Lett. B* **459**, 667 (1999), [arXiv:nucl-th/9906003](https://arxiv.org/abs/nucl-th/9906003).
- [34] K. Morita, S. Muroya, H. Nakamura, and C. Nonaka, Numerical analysis of two pion correlation based on a hydrodynamical model, *Phys. Rev. C* **61**, 034904 (2000), [arXiv:nucl-th/9906037](https://arxiv.org/abs/nucl-th/9906037).
- [35] C. Nonaka, E. Honda, and S. Muroya, (3+1)-dimensional relativistic hydrodynamical expansion of hot and dense matter in ultrarelativistic nuclear collision, *Eur. Phys. J. C* **17**, 663 (2000), [arXiv:hep-ph/0007187](https://arxiv.org/abs/hep-ph/0007187).
- [36] P. F. Kolb, P. Huovinen, U. W. Heinz, and H. Heiselberg, Elliptic flow at SPS and RHIC: From kinetic transport to hydrodynamics, *Phys. Lett. B* **500**, 232 (2001), [arXiv:hep-ph/0012137](https://arxiv.org/abs/hep-ph/0012137).
- [37] P. F. Kolb, J. Sollfrank, and U. W. Heinz, Anisotropic transverse flow and the quark hadron phase transition, *Phys. Rev. C* **62**, 054909 (2000), [arXiv:hep-ph/0006129](https://arxiv.org/abs/hep-ph/0006129).
- [38] P. Huovinen, P. F. Kolb, U. W. Heinz, P. V. Ruuskanen, and S. A. Voloshin, Radial and elliptic flow at RHIC: Further predictions, *Phys. Lett. B* **503**, 58 (2001), [arXiv:hep-ph/0101136](https://arxiv.org/abs/hep-ph/0101136).
- [39] T. Hirano, K. Morita, S. Muroya, and C. Nonaka, Hydrodynamical analysis of hadronic spectra in the 130 GeV/nucleon Au+Au collisions, *Phys. Rev. C* **65**, 061902 (2002), [arXiv:nucl-th/0110009](https://arxiv.org/abs/nucl-th/0110009).
- [40] K. Morita, S. Muroya, C. Nonaka, and T. Hirano, Comparison of space-time evolutions of hot / dense matter in $\sqrt{s_{NN}} = 17$ GeV and 130-GeV relativistic heavy ion collisions based on a hydrodynamical model, *Phys. Rev. C* **66**, 054904 (2002), [arXiv:nucl-th/0205040](https://arxiv.org/abs/nucl-th/0205040).
- [41] T. Hirano and K. Tsuda, Collective flow and two pion correlations from a relativistic hydrodynamic model with early chemical freezeout, *Phys. Rev. C* **66**, 054905 (2002), [arXiv:nucl-th/0205043](https://arxiv.org/abs/nucl-th/0205043).
- [42] P. Huovinen and P. V. Ruuskanen, Hydrodynamic Models for Heavy Ion Collisions, *Ann. Rev. Nucl. Part. Sci.* **56**, 163 (2006), [arXiv:nucl-th/0605008](https://arxiv.org/abs/nucl-th/0605008).
- [43] M. L. Miller, K. Reygers, S. J. Sanders, and P. Steinberg, Glauber modeling in high-energy nuclear collisions, *Annual Review of Nuclear and Particle Science* **57**, 205 (2007).
- [44] B. Schenke, P. Tribedy, and R. Venugopalan, Event-by-event gluon multiplicity, energy density, and eccentricities in ultrarelativistic heavy-ion collisions, *Physical Review C* **86**, [10.1103/physrevc.86.034908](https://doi.org/10.1103/physrevc.86.034908) (2012).
- [45] L. McLerran and R. Venugopalan, Computing quark and gluon distribution functions for very large nuclei, *Physical Review D* **49**, 2233 (1994).
- [46] L. McLerran and R. Venugopalan, Gluon distribution functions for very large nuclei at small transverse momentum, *Phys. Rev. D* **49**, 3352 (1994).
- [47] E. Iancu, A. Leonidov, and L. McLerran, The colour glass condensate: An introduction, *QCD Perspectives on Hot and Dense Matter*, 73 (2002).
- [48] M. Gyulassy and L. D. McLerran, Yang-Mills radiation in ultrarelativistic nuclear collisions, *Phys. Rev. C* **56**, 2219 (1997), [arXiv:nucl-th/9704034](https://arxiv.org/abs/nucl-th/9704034).
- [49] Y. V. Kovchegov and D. H. Rischke, Classical gluon radiation in ultrarelativistic nucleus-nucleus collisions, *Phys. Rev. C* **56**, 1084 (1997), [arXiv:hep-ph/9704201](https://arxiv.org/abs/hep-ph/9704201).
- [50] A. Krasnitz and R. Venugopalan, Non-perturbative computation of gluon mini-jet production in nuclear collisions at very high energies, *Nuclear Physics B* **557**, 237 (1999).
- [51] A. Krasnitz, Y. Nara, and R. Venugopalan, Gluon production in the color glass condensate model of collisions of ultrarelativistic finite nuclei, *Nuclear Physics A* **717**, 268 (2003).
- [52] A. Dumitru and L. D. McLerran, How protons shatter colored glass, *Nucl. Phys. A* **700**, 492 (2002), [arXiv:hep-ph/0105268](https://arxiv.org/abs/hep-ph/0105268).
- [53] M. Alvioli, H. Drescher, and M. Strikman, A monte carlo generator of nucleon configurations in complex nuclei including nucleon-nucleon correlations, *Physics Letters B* **680**, 225 (2009).
- [54] R. Dalal and I. J. D. MacGregor, Nucleon-nucleon correlations inside atomic nuclei: synergies, observations and theoretical models (2022), [arXiv:2210.06114 \[nucl-th\]](https://arxiv.org/abs/2210.06114).
- [55] H. Kowalski and D. Teaney, Impact parameter dipole saturation model, *Physical Review D* **68**, [10.1103/physrevd.68.114005](https://doi.org/10.1103/physrevd.68.114005) (2003).
- [56] A. H. Rezaeian, M. Siddikov, M. Van de Klundert, and R. Venugopalan, Analysis of combined HERA data in the impact-parameter dependent saturation model, *Phys. Rev. D* **87**, 034002 (2013).
- [57] G. Altarelli and G. Parisi, Asymptotic Freedom in Parton Language, *Nucl. Phys. B* **126**, 298 (1977).
- [58] Y. L. Dokshitzer, Calculation of the Structure Functions for Deep Inelastic Scattering and e^+e^- Annihilation by Perturbation Theory in Quantum Chromodynamics., *Sov. Phys. JETP* **46**, 641 (1977).
- [59] F. Gelis, [Dglap equations solver](https://arxiv.org/abs/hep-ph/0006077).
- [60] A. H. Mueller, Small x Behavior and Parton Saturation: A QCD Model, *Nucl. Phys. B* **335**, 115 (1990).
- [61] A. Kovner, L. McLerran, and H. Weigert, Gluon production at high transverse momentum in the mclerran-venugopalan model of nuclear structure functions, *Physical Review D* **52**, 3809 (1995).
- [62] A. Kovner, L. McLerran, and H. Weigert, Gluon production from non-abelian weizsäcker-williams fields in nucleus-nucleus collisions, *Phys. Rev. D* **52**, 6231 (1995).
- [63] D. N. Blaschke, F. Gieres, M. Reboud, and M. Schweda, The energy-momentum tensor(s) in classical gauge theories, *Nuclear Physics B* **912**, 192 (2016), mathematical Foundations of Quantum Field Theory: A volume dedicated to the Memory of Raymond Stora.
- [64] A. Bazavov, P. Petreczky, and J. Weber, Equation of state in 2+1 flavor QCD at high temperatures, *Physi-*

- cal Review D **97**, [10.1103/physrevd.97.014510](https://arxiv.org/abs/10.1103/physrevd.97.014510) (2018).
- [65] P. F. Kolb and U. W. Heinz, Hydrodynamic description of ultrarelativistic heavy ion collisions, *Quark Gluon Plasma 3*, 634 (2003), [arXiv:nucl-th/0305084](https://arxiv.org/abs/nucl-th/0305084).
- [66] S. Jeon and U. Heinz, Introduction to hydrodynamics, *International Journal of Modern Physics E* **24**, 1530010 (2015).
- [67] B. Schenke, S. Jeon, and C. Gale, Elliptic and triangular flow in event-by-event (3+1)D viscous hydrodynamics, *Phys. Rev. Lett.* **106**, 042301 (2011), [arXiv:1009.3244 \[hep-ph\]](https://arxiv.org/abs/1009.3244).
- [68] G. S. Denicol, S. Jeon, and C. Gale, Transport coefficients of bulk viscous pressure in the 14-moment approximation, *Physical Review C* **90**, [10.1103/physrevc.90.024912](https://arxiv.org/abs/10.1103/physrevc.90.024912) (2014).
- [69] A. Pandav, D. Mallick, and B. Mohanty, Search for the QCD critical point in high energy nuclear collisions, *Progress in Particle and Nuclear Physics* **125**, 103960 (2022).
- [70] Y. Yin, The QCD critical point hunt: emergent new ideas and new dynamics (2018), [arXiv:1811.06519 \[nucl-th\]](https://arxiv.org/abs/1811.06519).
- [71] X. Luo and N. Xu, Search for the QCD critical point with fluctuations of conserved quantities in relativistic heavy-ion collisions at RHIC: an overview, *Nuclear Science and Techniques* **28**, [10.1007/s41365-017-0257-0](https://arxiv.org/abs/10.1007/s41365-017-0257-0) (2017).
- [72] F. Cooper and G. Frye, Single-particle distribution in the hydrodynamic and statistical thermodynamic models of multiparticle production, *Phys. Rev. D* **10**, 186 (1974).
- [73] H. Grad, On the kinetic theory of rarefied gases, *Communications on Pure and Applied Mathematics* **2**, 331 (1949).
- [74] A. Monnai and T. Hirano, Effects of bulk viscosity at freezeout, *Phys. Rev. C* **80**, 054906 (2009).
- [75] W. Israel and J. Stewart, Transient relativistic thermodynamics and kinetic theory, *Annals of Physics* **118**, 341 (1979).
- [76] B. Schenke, P. Tribedy, and R. Venugopalan, Initial-state geometry and fluctuations in Au + Au, Cu + Au, and U + U collisions at energies available at the BNL Relativistic Heavy Ion Collider, *Phys. Rev. C* **89**, 064908 (2014).
- [77] L.-M. Liu, C.-J. Zhang, J. Xu, J. Jia, and G.-X. Peng, Free spectator nucleons in ultracentral relativistic heavy-ion collisions as a probe of neutron skin, *Physical Review C* **106**, [10.1103/physrevc.106.034913](https://arxiv.org/abs/10.1103/physrevc.106.034913) (2022).
- [78] G. Giacalone, G. Nijs, and W. van der Schee, Determination of the neutron skin of ^{208}Pb from ultrarelativistic nuclear collisions (2023), [arXiv:2305.00015 \[nucl-th\]](https://arxiv.org/abs/2305.00015).
- [79] N. Borghini, P. M. Dinh, and J.-Y. Ollitrault, New method for measuring azimuthal distributions in nucleus-nucleus collisions, *Physical Review C* **63**, [10.1103/physrevc.63.054906](https://arxiv.org/abs/10.1103/physrevc.63.054906) (2001).
- [80] A. Bilandzic, R. Snellings, and S. Voloshin, Flow analysis with cumulants: Direct calculations, *Physical Review C* **83**, [10.1103/physrevc.83.044913](https://arxiv.org/abs/10.1103/physrevc.83.044913) (2011).
- [81] G. Giacalone, F. G. Gardim, J. Noronha-Hostler, and J.-Y. Ollitrault, Skewness of mean transverse momentum fluctuations in heavy-ion collisions, *Physical Review C* **103**, [10.1103/physrevc.103.024910](https://arxiv.org/abs/10.1103/physrevc.103.024910) (2021).
- [82] P. Bożek, Transverse-momentum-flow correlations in relativistic heavy-ion collisions, *Physical Review C* **93**, [10.1103/physrevc.93.044908](https://arxiv.org/abs/10.1103/physrevc.93.044908) (2016).
- [83] M. Abdallah, B. Aboona, J. Adam, *et al.*, Pion, kaon, and (anti)proton production in U+U collisions at 193 GeV measured with the STAR detector, *Physical Review C* **107**, [10.1103/physrevc.107.024901](https://arxiv.org/abs/10.1103/physrevc.107.024901) (2023).
- [84] S. S. Adler, S. Afanasiev, C. Aidala, N. N. Ajitanand, *et al.*, Identified charged particle spectra and yields in Au+Au Collisions at $\sqrt{s_{NN}} = 200$ GeV, *Physical Review C* **69**, [10.1103/physrevc.69.034909](https://arxiv.org/abs/10.1103/physrevc.69.034909) (2004).
- [85] B. I. Abelev, M. M. Aggarwal, Z. Ahammed, B. D. Anderson, *et al.*, Systematic Measurements of Identified Particle Spectra in pp, d+Au and Au+Au Collisions from STAR, *Physical Review C* **79**, [10.1103/physrevc.79.034909](https://arxiv.org/abs/10.1103/physrevc.79.034909) (2009).
- [86] S. Pratt, E. Sangaline, P. Sorensen, and H. Wang, Constraining the equation of state of superhadronic matter from heavy-ion collisions, *Physical Review Letters* **114**, [10.1103/physrevlett.114.202301](https://arxiv.org/abs/10.1103/physrevlett.114.202301) (2015).
- [87] A. Kumar and T. Toll, Investigating the structure of gluon fluctuations in the proton with incoherent diffraction at HERA, *The European Physical Journal C* **82**, [10.1140/epjc/s10052-022-10774-3](https://arxiv.org/abs/10.1140/epjc/s10052-022-10774-3) (2022).
- [88] S. Collaboration, Imaging shapes of atomic nuclei in high-energy nuclear collisions (2024), [arXiv:2401.06625 \[nucl-ex\]](https://arxiv.org/abs/2401.06625).
- [89] N. Fortier, S. Jeon, and C. Gale, Comparisons and Predictions for Collisions of deformed ^{238}U nuclei at $\sqrt{s_{NN}} = 193$ GeV (2023), [arXiv:2308.09816v1 \[nucl-th\]](https://arxiv.org/abs/2308.09816v1).
- [90] J. Jia, Probing triaxial deformation of atomic nuclei in high-energy heavy ion collisions, *Physical Review C* **105**, [10.1103/physrevc.105.044905](https://arxiv.org/abs/10.1103/physrevc.105.044905) (2022).
- [91] S. Acharya, F. Tolares-Acosta, D. Adamová, J. Adolfsen, *et al.*, Centrality and pseudorapidity dependence of the charged-particle multiplicity density in xe-xe collisions at 5.44 tev, *Physics Letters B* **790**, 35 (2019).
- [92] G. Colò, Nuclear density functional theory, *Advances in Physics: X* **5**, 1740061 (2020), <https://doi.org/10.1080/23746149.2020.1740061>.